Haemorheology in dilute, semi-dilute and dense suspensions of red blood cells

Naoki Takeishi[1,†], Marco E. Rosti[2], Yohsuke Imai[3], Shigeo Wada[1] and Luca Brandt[2]

[1]Graduate School of Engineering Science, Osaka University, 1-3 Machikaneyama, Toyonaka, Osaka 560-8531, Japan

[2]Linné Flow Centre and SeRC (Swedish e-Science Research Centre), KTH Mechanics, SE 100 44 Stockholm, Sweden

[3]Graduate School of Engineering, Kobe University, 1-1 Rokkodai, Nada, Kobe 657-8501, Japan

We present a numerical analysis of the rheology of a suspension of red blood cells (RBCs) in a wall-bounded shear flow. The flow is assumed as almost inertialess. The suspension of RBCs, modelled as biconcave capsules whose membrane follows the Skalak constitutive law, is simulated for a wide range of viscosity ratios between the cytoplasm and plasma, $\lambda = 0.1$–10, for volume fractions up to $\phi = 0.41$ and for different capillary numbers (Ca). Our numerical results show that an RBC at low Ca tends to orient to the shear plane and exhibits so-called rolling motion, a stable mode with higher intrinsic viscosity than the so-called tumbling motion. As Ca increases, the mode shifts from the rolling to the swinging motion. Hydrodynamic interactions (higher volume fraction) also allow RBCs to exhibit tumbling or swinging motions resulting in a drop of the intrinsic viscosity for dilute and semi-dilute suspensions. Because of this mode change, conventional ways of modelling the relative viscosity as a polynomial function of ϕ cannot be simply applied in suspensions of RBCs at low volume fractions. The relative viscosity for high volume fractions, however, can be well described as a function of an effective volume fraction, defined by the volume of spheres of radius equal to the semi-middle axis of a deformed RBC. We find that the relative viscosity successfully collapses on a single nonlinear curve independently of λ except for the case with $Ca \geqslant 0.4$, where the fit works only in the case of low/moderate volume fraction, and fails in the case of a fully dense suspension.

Key words: blood flow, capsule/cell dynamics, suspensions

1. Introduction

The viscosity of blood is a basic biological parameter affecting the blood flow both in large arteries and in microcirculations, and hence studies of haemorheology from the single-cell level to macroscale blood flow have been conducted for many decades (Pedley 1980; Mohandas & Gallagher 2008; Secomb 2017). Since human blood is a dense suspension consisting of 55 % fluid (plasma) and 45 % blood cells,

† Email address for correspondence: ntakeishi@me.es.osaka-u.ac.jp

with over 98 % of the cells being red blood cells (RBCs), hydrodynamic interactions of individual RBCs are of fundamental importance for haemorheology. Despite a number of studies of haemorheology, much is still unknown, in particular about how the single-cell behaviour relates to the behaviour in suspensions and then rheology. Therefore, the objective of this study is to clarify the behaviour of individual RBCs from dilute to dense suspensions, and to elucidate the relationship between behaviours of individual RBCs and haemorheology.

Clarifying the cellular-scale dynamics allows us to build precise continuum models of suspensions (Ishikawa 2012; Henríquez-Rivera, Sinha & Graham 2015), and potentially leads us to novel diagnoses about patients with blood diseases (Ito *et al.* 2017). Therefore, researchers have made every effort to reveal the dynamics of single RBCs as well as the rheological description of blood flow. By means of experimental observations, the dynamics of single RBCs has been well investigated. For example, RBCs subjected to a low shear rate exhibit rigid-body-like flipping, the so-called tumbling motion (Schmid-Schönbein & Wells 1969; Fischer 2004; Dupire, Abkarian & Viallat 2010), and wheel-like rotation, the so-called rolling motion (Dupire, Socol & Viallat 2012; Lanotte *et al.* 2016), while RBCs subjected to high shear rates exhibit the so-called tank-treading motion (Schmid-Schönbein & Wells 1969; Fischer, Stöhr-Liesen & Schmid-Schönbein 1978; Fischer 2004). The swinging motion was introduced by Abkarian, Faivre & Viallat (2007) as an oscillating orientation of tank-treading motion in the case of relatively low viscosity ratio $\lambda \sim 0.5$. By means of numerical simulations, it has been observed that the dynamics transitions from rolling/tumbling to kayaking (or oscillating–swinging) and swinging, following tank-treading motions for a wide range of viscosity ratios $(0.1 < \lambda < 10)$ (Cordasco & Bagchi 2014; Sinha & Graham 2015). Moreover, recent experimental and numerical studies demonstrated that a rolling or tumbling RBC can shift to a stomatocyte first and finally attaining polylobed shapes (or multilobes) as the shear rate increases with relatively high viscosity ratios $(\lambda \sim 3\text{--}5)$ (Lanotte *et al.* 2016; Mauer *et al.* 2018). Despite these insights, it is not known how the various motions of individual RBCs affect the bulk suspension rheology.

The rheological description of suspensions, especially of rigid particles, was addressed in the pioneering work by Batchelor (1970), showing that stress due to the presence of particles is evaluated using a particle stress tensor, which can be expressed as a summation of stresslets in a domain. Pozrikidis (1992) analytically derived the effective stresslet of a deformable capsule consisting of an internal fluid enclosed by a thin elastic membrane. It is known that the usual distribution of haemoglobin concentration in individual RBCs ranges from 27 to 37 g dl^{-1} corresponding to the internal fluid viscosity being $\mu_1 = 5\text{--}15$ cP $(=5\text{--}15 \times 10^{-3}$ Pa s) (Mohandas & Gallagher 2008), while the normal plasma (external fluid) viscosity is $\mu_0 = 1.1\text{--}1.3$ cP $(=1.1\text{--}1.3 \times 10^{-3}$ Pa s) for plasma at 37 °C (Harkness & Whittington 1970). If the plasma viscosity is set to be $\mu_0 = 1.2$ cP, the physiologically relevant viscosity ratio can be taken as $\lambda \, (=\mu_1/\mu_0) = 4.2\text{--}12.5$. At the single-cell level, the effect of viscosity ratio λ on steady motions has been well investigated (Cordasco, Yazdani & Bagchi 2014; Mauer *et al.* 2018). In suspensions, numerical studies of the behaviours of deformable particles modelled as neo-Hookean spherical capsules (Clausen, Reasor Jr & Aidun 2011; Kumar, Henríquez-Rivera & Graham 2014; Matsunaga *et al.* 2016) or as viscoelastic materials (Rosti & Brandt 2018; Rosti, Brandt & Mitra 2018) have been conducted, while numerical studies of the behaviours of RBCs modelled as deformable biconcave capsules are still limited (Fedosov *et al.* 2011; Reasor Jr, Clausen & Aidun 2013; Gross, Krüger & Varnik 2014; Lanotte *et al.* 2016), where

the shear-thinning behaviour of a suspension of RBCs was systematically investigated. However, it remains unclear how the viscosity ratio λ affects the bulk suspension rheology of RBCs.

Nowadays, a rheological description of blood is important considering the fast-increasing worldwide incidence of diabetes mellitus. Skovborg *et al.* (1966) measured the viscosity of blood from diabetic patients, and found that it was approximately 20 % higher than in controls. Elevated blood viscosity was also found in other haematologic disorders, e.g. multiple myeloma (Dintenfass & Somer 1975; Somer 1987) and sickle cell disease (Embury *et al.* 1984; Evans, Mohandas & Leung 1984). An experimental study using a coaxial cylinder viscometer revealed that the blood from patients with sickle cell anaemia, which is an inherited blood disorder exhibiting heterogeneous cell morphology, had higher haemoglobin concentration resulting in abnormal rheology (Chien, Usami & Bertles 1970; Usami *et al.* 1975; Kaul & Xue 1991). Numerical study of two-body interactions of RBCs also concluded that the viscosity ratio is one of the most important parameters in haemorheology for the dilute and the semi-dilute regimes (Omori *et al.* 2014). As a conventional rheological description, the relative viscosity μ_{re} is often modelled as a polynomial function of the volume fraction ϕ. For example, Einstein (1911) proposed the viscosity law for a dilute suspension of rigid particles: $\mu_{re} = 1 + 2.5\phi$; while Taylor (1932) proposed a modified law for particles including internal fluid: $\mu_{re} = 1 + 2.5\tilde{\lambda}\phi$, where $\tilde{\lambda}$ is Taylor's factor defined as $\tilde{\lambda} = (\lambda + 0.4)/(\lambda + 1)$. More recently, such a polynomial approach has been applied to dense suspensions of deformable particles, with high-order terms of ϕ (Matsunaga *et al.* 2016; Rosti & Brandt 2018). However, a polynomial law for dense suspensions of non-spherical deformable particles such as RBCs is still missing due to the complexity of the phenomenon.

To obtain a rheological description of RBC suspensions, we investigate the effect of a wide range of viscosity ratios $\lambda = 0.1$–10, non-dimensional shear rates (capillary number, Ca) and volume fractions ϕ. We performed numerical simulations to study the behaviour of RBCs subjected to various Ca in wall-bounded shear flow from dilute suspensions ($\phi = 6 \times 10^{-4}$; single RBC level) to dense suspensions ($\phi = 0.41$). The contribution of individual deformed RBCs to the bulk suspension rheology is quantified by the stresslet tensor (Batchelor 1970). The RBC is modelled as a biconcave capsule, whose membrane follows the Skalak constitutive law (Skalak *et al.* 1973). Since this problem requires heavy computational resources, we resort to graphics processing unit (GPU) computing, using the lattice-Boltzmann method (LBM) for the inner and outer fluid and the finite-element method (FEM) to follow the deformation of the RBC membrane. The models have been successfully applied to the analysis of hydrodynamic interactions between RBCs and leukocytes (Takeishi *et al.* 2014), circulating tumour cells (Takeishi *et al.* 2015) and microparticles/platelets (Takeishi & Imai 2017; Takeishi, Imai & Wada 2019) in channel flows.

The remainder of this paper is organized as follows. Section 2 gives the problem statement and numerical methods. Section 3 presents the numerical results for single RBCs and semi-dilute/dense suspensions. Section 4 presents a discussion and comparison between our numerical results and previous experimental/numerical results. This is followed by a summary of the main conclusions in § 5. The validation of our numerical model is described in appendix A.

2. Problem statement

2.1. *Flow and cell models*

We consider a cellular flow consisting of plasma and RBCs with radius a in a rectangular box of size $16a \times 10a \times 16a$ along the spanwise x, wall-normal y and

streamwise z directions, with a resolution of 8 fluid lattices per radius of RBC. Although the domain size used here has been shown to be adequate for investigating suspensions of rigid and deformable spherical particles in previous studies (Picano *et al.* 2013; Rosti & Brandt 2018), we preliminarily checked its effect for RBCs as well as the effect of the wall (§§ A.2 and A.3). An RBC is modelled as a biconcave capsule of a Newtonian fluid enclosed by a thin elastic membrane, with a major diameter 8 μm ($=2a$) and maximum thickness 2 μm ($=a/2$). Although some recent numerical studies argued about the stress-free shape of RBCs (Peng, Mashayekh & Zhu 2014; Tsubota, Wada & Liu 2014; Sinha & Graham 2015), we define the initial shape of an RBC as a biconcave shape.

The shear flow is generated by moving the top and bottom walls located at $y = \pm H/2$ with constant velocity $U_{wall} = \pm\dot{\gamma}H/2$, where H ($=10a$) is the domain height and $\dot{\gamma}$ ($=U_c/a$) is the shear rate defined using the characteristic velocity U_c. Periodic boundary conditions are imposed on the two homogeneous directions (x and z directions). The cytoplasmic viscosity is taken to be $\mu_1 = 6.0 \times 10^{-3}$ Pa s, which is five times higher than the plasma viscosity: $\mu_0 = 1.2 \times 10^{-3}$ Pa s (Harkness & Whittington 1970). Hence, in our study, the physiologically relevant viscosity ratio is set to be λ ($=\mu_1/\mu_0) = 5$, and the range of viscosity ratios $\lambda = 0.1$–10 are considered. The problem is characterized by the capillary number (Ca) as

$$Ca = \frac{\mu_0 U_c}{G_s} = \frac{\mu_0 \dot{\gamma} a}{G_s}, \tag{2.1}$$

where G_s is the surface shear elastic modulus. To counter the computational costs, we set $Re = \rho U_c a/\mu_0 = 0.2$, where ρ is the plasma density. This value well represents capsule dynamics in unbounded shear flows solved by the boundary integral method (BIM) in Stokes flow (Omori *et al.* 2012; Matsunaga *et al.* 2016) (see also §§ A.1 and A.3). In this study, the range of $Ca = 0.05$–1.2 is considered covering typical venule wall-shear rate of 333 s^{-1} (Koutsiaris, Tachmitzi & Batis 2013), corresponding to $Ca = 0.4$, and arteriole wall-shear rate of 670 s^{-1} (Koutsiaris *et al.* 2007), corresponding to $Ca = 0.8$.

The membrane is modelled as an isotropic and hyperelastic material. The surface deformation gradient tensor $\boldsymbol{F}_s$ is given by

$$d\boldsymbol{x}_m = \boldsymbol{F}_s \cdot dX_m, \tag{2.2}$$

where X_m and $\boldsymbol{x}_m$ are the membrane material points of the reference and deformed states, respectively. The local deformation of the membrane can be measured by the Green–Lagrange strain tensor

$$\boldsymbol{E} = \tfrac{1}{2}(\boldsymbol{C} - \boldsymbol{I}_s), \tag{2.3}$$

where $\boldsymbol{I}_s$ is the tangential projection operator. The two invariants of the in-plane strain tensor $\boldsymbol{E}$ can be given by

$$I_1 = \lambda_1^2 + \lambda_2^2 - 2, \quad I_2 = \lambda_1^2 \lambda_2^2 - 1 = J_s^2 - 1, \tag{2.4a,b}$$

where λ_1 and λ_2 are the principal extension ratios. The Jacobian $J_s = \lambda_1 \lambda_2$ expresses the ratio of the deformed to the reference surface areas. The elastic stresses in an infinitely thin membrane are replaced by elastic tensions. The Cauchy tension $\boldsymbol{T}$ can be related to an elastic strain energy per unit area, $w_s(I_1, I_2)$:

$$\boldsymbol{T} = \frac{1}{J_s} \boldsymbol{F}_s \cdot \frac{\partial w_s(I_1, I_2)}{\partial \boldsymbol{E}} \cdot \boldsymbol{F}_s^{\mathrm{T}}, \tag{2.5}$$

where the strain energy function w_s satisfies the Skalak (SK) constitutive law (Skalak *et al.* 1973)

$$w_s^{SK} = \frac{G_s}{4}(I_1^2 + 2I_1 - 2I_2 + CI_2^2), \tag{2.6}$$

with C being a coefficient representing the area incompressibility. In this study, we set $G_s = 4$ μN m^{-1} and $C = 10^2$. Bending resistance is also considered (Li *et al.* 2005), with a bending modulus $k_b = 5.0 \times 10^{-19}$ J (Puig-de-Morales-Marinkovic *et al.* 2007). These values successfully reproduce the deformation of RBCs in shear flow and also the thickness of the cell-depleted peripheral layer; see § A.1 (Takeishi *et al.* 2014).

2.2. *Numerical method*

The in-plane elastic tensions $\boldsymbol{T}$ are obtained from the SK constitutive law (2.6). Neglecting inertial effects on the membrane deformation, the static local equilibrium equation of the membrane is given by

$$\nabla_s \cdot \boldsymbol{T} + \boldsymbol{q} = \boldsymbol{0}, \tag{2.7}$$

where ∇_s is the surface gradient operator. Based on the virtual work principle, the above strong form (2.7) can be rewritten in weak form as

$$\int_S \hat{\boldsymbol{u}} \cdot \boldsymbol{q} \, \mathrm{d}S = \int_S \hat{\boldsymbol{\epsilon}} : \boldsymbol{T} \, \mathrm{d}S, \tag{2.8}$$

where $\hat{\boldsymbol{u}}$ and $\hat{\boldsymbol{\epsilon}} = (\nabla_s \hat{\boldsymbol{u}} + \nabla_s \hat{\boldsymbol{u}}^{\mathrm{T}})/2$ are the virtual displacement and virtual strain, respectively. The FEM is used to solve (2.8) and obtain the load $\boldsymbol{q}$ acting on the membrane (see also Walter *et al.* 2010).

The LBM based on the D3Q19 model (Chen & Doolen 1998; Dupin *et al.* 2007) is used to solve the fluid velocity field in the plasma and cytoplasm within the RBC membrane. In the LBM, the macroscopic flow is obtained by collision and streaming of hypothetical particles described by the lattice-Boltzmann Bhatnagar–Gross–Krook equation (Bhatnagar, Gross & Krook 1954), which is given as

$$f_i(\boldsymbol{x}_f + \boldsymbol{c}_i \Delta t, t + \Delta t) - f(\boldsymbol{x}_f, t) = -\frac{1}{\tau}[f_i(\boldsymbol{x}_f, t) - f_i^{eq}(\boldsymbol{x}_f, t)] + F_i \Delta t, \tag{2.9}$$

where f_i is the particle distribution function for particles with velocity $\boldsymbol{c}_i$ ($i = 0$–18) at the fluid node $\boldsymbol{x}_f$, Δt is the time step size, f_i^{eq} is the equilibrium distribution function and τ is the non-dimensional relaxation time. The external force term F_i can be written as

$$F_i = \left(1 - \frac{1}{2\tau}\right) w_i \left[\frac{\boldsymbol{c}_i - \boldsymbol{v}}{c_s^2} + \frac{(\boldsymbol{c}_i \cdot \boldsymbol{v})}{c_s^4}\right] \cdot \boldsymbol{F}(\boldsymbol{x}_f), \tag{2.10}$$

where $c_s = \Delta x_f/(\sqrt{3}\Delta t)$ is the speed of sound. The external force $\boldsymbol{F}(\boldsymbol{x}_f)$ is a distributed force applied from the membrane material points with the immersed boundary method (IBM) (Peskin 2002). The particle velocity $\boldsymbol{c}_i$ is written by using the time-step size Δt and the lattice size Δx_f as

$$\boldsymbol{c}_i = c_i^I \frac{\Delta x_f}{\Delta t} \boldsymbol{e}_I, \tag{2.11}$$

where e_I is the Cartesian basis. The equilibrium distribution function is given by

$$f_i^{eq}(x_f, t) = \rho w_i \left[1 + \frac{v \cdot c_i}{c_s^2} + \frac{(v \otimes v) : (c_i \otimes c_i - c_s^2 I)}{2c_s^4} \right], \tag{2.12}$$

where w_i is the weight ($w_i = 0$ for $i = 0$, $w_i = 1/18$ for the non-diagonal directions and $w_i = 1/36$ for the diagonal directions) and I is the identity tensor. The macroscopic variables ρ and v are defined as

$$\rho = \sum_i f_i, \tag{2.13}$$

$$\rho v = \sum_i c_i f_i + \frac{1}{2} F(x_f) \Delta t. \tag{2.14}$$

In the IBM (Peskin 2002), the membrane force $f(x_m)$ at the membrane node x_m is distributed to the neighbouring fluid nodes x_f, and the external force $F(x_f)$ in (2.10) is computed as

$$F(x_f) = \sum_m D(x_f - x_m) f(x_m), \tag{2.15}$$

where $D(x)$ is a smoothed delta function approximating the Dirac delta function, given by

$$D(x) = \begin{cases} \dfrac{1}{64\Delta x_f^3} \displaystyle\prod_{k=1}^{3} \left(1 + \cos \dfrac{\pi x_k}{2\Delta x_f} \right) & \text{if } |x_k| \leqslant 2\Delta x_f, \ x_1 = x, \ x_2 = y, \ x_3 = z, \\ 0 & \text{otherwise.} \end{cases} \tag{2.16}$$

The velocity at the membrane node $v(x_m)$ is obtained by interpolating the velocities at the fluid nodes as

$$v(x_m) = \sum_f D(x_f - x_m) v(x_f). \tag{2.17}$$

The membrane node x_m is updated by Lagrangian tracking with the no-slip condition, i.e.

$$\frac{dx_m}{dt} = v(x_m). \tag{2.18}$$

The explicit fourth-order Runge–Kutta method is used for the time integration. Note that by using our coupling method of LBM and IBM, the hydrodynamic interaction of individual RBCs is solved without modelling a non-hydrodynamic inter-membrane repulsive force in the case of vanishing inertia, as also shown in § A.3.

The viscosity of a LB node x_f is found using the volume of fluid $\psi(x_f)$ ($0 \leqslant \psi \leqslant 1$) of the internal fluid of the RBCs:

$$\mu = (1 - \psi)\mu_0 + \psi \mu_1 = \{1 + (\lambda - 1)\psi\}\mu_0, \tag{2.19}$$

and the kinematic viscosity as

$$\nu = \frac{\mu}{\rho} = \{1 + (\lambda - 1)\psi\} \frac{\mu_0}{\rho} = \frac{2\tau - 1}{2} c_s^2 \Delta t = \frac{2\tau - 1}{6} \frac{\Delta r^2}{\Delta t}. \tag{2.20}$$

To update the viscosity on the fluid lattice, we consider the volume-of-fluid function ψ, which is governed by an advection equation:

$$\frac{\partial \psi}{\partial t} + \boldsymbol{\nabla} \cdot (\boldsymbol{v}\psi) - \psi \boldsymbol{\nabla} \cdot \boldsymbol{v} = 0. \tag{2.21}$$

Equation (2.21) is solved by the THINC/WLIC (tangent of hyperbola for interface capturing/weighted line interface calculation) method (Yokoi 2007), which is a combination of the THINC scheme and the WLIC method. As a characteristic function of the THINC scheme, the piecewise modified hyperbolic tangent function (Xiao, Honma & kono 2005) is used. In the WLIC formulation, the interface is reconstructed by taking an average of the interfaces along the x, y and z coordinates with weights calculated from the surface normal. To counter the divergence between the interface of ψ and the membrane surface, we also solve the Poisson equation of the indicator function $\mathcal{I}(\boldsymbol{x}_f)$ used in the front-tracking method (Unverdi & Tryggvason 1992):

$$\nabla^2 \mathcal{I}(\boldsymbol{x}_f) = \boldsymbol{\nabla} \cdot \boldsymbol{G}(\boldsymbol{x}_f), \tag{2.22}$$

where $\mathcal{I} = 1$ in the interior of a cell and $\mathcal{I} = 0$ outside a cell, and $\boldsymbol{G}(\boldsymbol{x}_f)$ is described by the smoothed delta function (2.16):

$$\boldsymbol{G}(\boldsymbol{x}_f) = \boldsymbol{\nabla}\mathcal{I}(\boldsymbol{x}_f) = \sum_e D(\boldsymbol{x}_f - \boldsymbol{x}_e)\boldsymbol{n}_e \Delta s_e, \tag{2.23}$$

where $\boldsymbol{n}_e$ is the outward unit normal vector to an element with the area Δs_e, whose centroid is $\boldsymbol{x}_e$. To speed up the numerical simulations, we only solve the Poisson equation of the indicator function every 10 000 steps. Our methods are validated for different viscosity ratios by comparing the values of the Taylor parameter of deformed spherical capsules with those reported in Foessel *et al.* (2011), as detailed in §A.1. A volume constraint is implemented to counteract the accumulation of small errors in the volume of the individual cells (Freund 2007): in our simulation, the volume error is always maintained lower than $1.0 \times 10^{-3}\,\%$, as tested and validated in our previous study of cell adhesion (Takeishi *et al.* 2016).

All numerical procedures are fully implemented on GPU to accelerate the numerical simulation (Miki *et al.* 2012). The mesh size of the LBM for the fluid solution is set to be 250 nm, and that of the finite elements describing the membrane is approximately 250 nm (an unstructured mesh with 5120 elements is used for the FEM). This resolution has been shown to successfully represent single- and multi-cellular dynamics (Takeishi *et al.* 2014); also, the results of multi-cellular dynamics do not change with twice the resolution of both the fluid mesh and membrane mesh (see also Takeishi *et al.* 2014).

2.3. *Analysis of capsule suspensions*

For the following analysis, the behaviour of RBCs subjected to shear flow is quantified by two different orientation angles θ and Ψ as shown in figure 1(*a,b*), where θ is the angle between the major axis of the deformed RBC and the shear direction and Ψ is the angle between the vortex axis and the normal vector at the initial concave node point (green dot in figure 1*a,b*). In suspensions of RBCs, the ensemble average of these orientation angles is calculated as

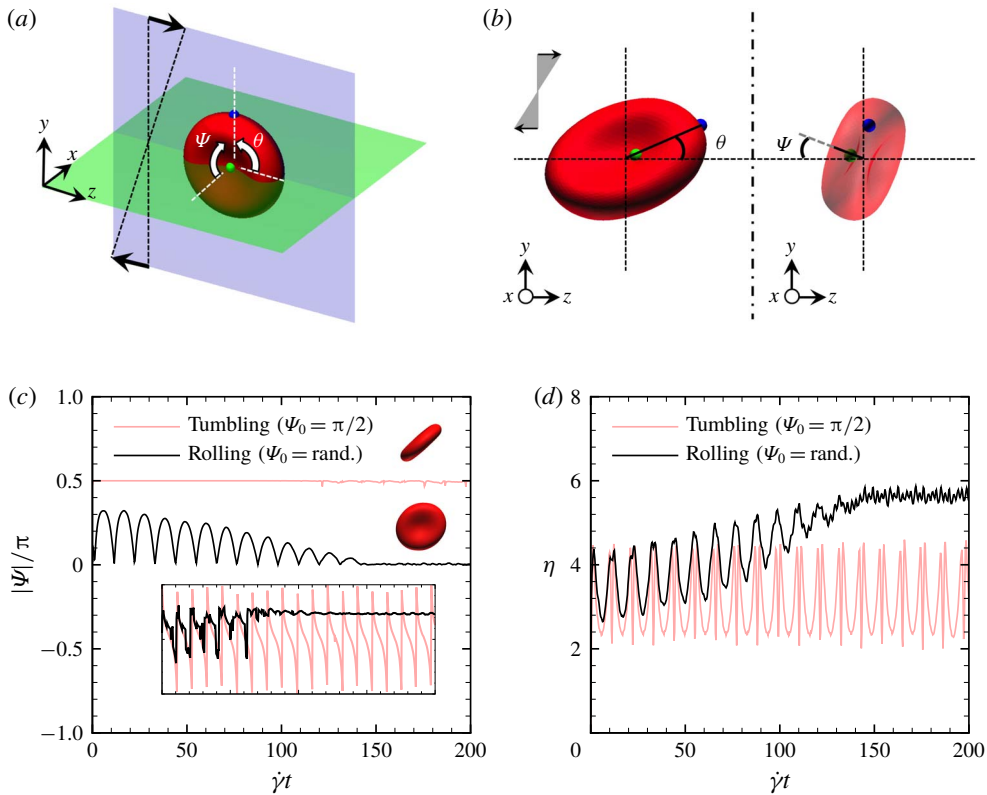$$\langle \xi \rangle = \frac{1}{MN} \sum_m^M \sum_n^N \xi^{m,n} \quad (\xi = \theta \text{ or } \Psi), \tag{2.24}$$

FIGURE 1. (Colour online) (*a*,*b*) Schematic of the three-dimensional orientation of an RBC (*a*). The shear flow is driven along the z direction by moving the top and bottom walls. Periodic boundary conditions are imposed on the flow (z direction) and vortex (x direction) directions. Coloured dots on the membrane denote material points to measure the RBC orientation, which is defined by the angle θ between the major axis of the deformed RBC and the shear direction and the angle Ψ between the vortex axis and the green dot (*b*). (*c*) Time history of the orientation angles Ψ and θ for different motions; tumbling motion (light red line) for RBC initial orientation $\Psi_0 = \pi/2$ and rolling motion (black line) for random initial state, i.e. $\Psi_0 = $ rand. The upper inset represents the tumbling motion of an RBC (see the supplementary movie 1, available at https://doi.org/10.1017/jfm.2019.393) and the lower inset the rolling motion of an RBC (see the supplementary movie 2). (*d*) Time history of the intrinsic viscosity η ($=\mu_{sp}/\phi$) for tumbling (light red line) and rolling (black line) motions. The results are obtained with $\lambda = 5$ at $Ca = 0.05$.

where M and N are the number of time steps and capsules (RBCs), respectively. Time average starts after the non-dimensional time $\dot{\gamma}t = 40$ to reduce the influence of the initial conditions, and continues to over $\dot{\gamma}t = 100$.

For the analysis of the suspension rheology, we consider the contribution of the suspended particles to the bulk viscosity in terms of the particle stress tensor $\boldsymbol{\Sigma}^{(p)}$ (Batchelor 1970):

$$\boldsymbol{\Sigma}^{(p)} = \frac{1}{V} \sum_{i}^{N} \boldsymbol{S}_i, \tag{2.25}$$

where V is the volume of the domain and S_i the stresslet of the ith particle (capsule and RBC in the present study). Pozrikidis (1992) analytically derived the stresslet of a deformable capsule for any viscosity ratio:

$$S_i = \int \left[\tfrac{1}{2}(x \otimes \hat{q} + \hat{q} \otimes x) - \mu_0(1 - \lambda)(v \otimes n + n \otimes v) \right] \mathrm{d}A_i, \qquad (2.26)$$

where x is the membrane position relative to the centre of the RBC, $\hat{q}$ the load acting on the membrane including a contribution of bending rigidity, n the surface normal vector, μ_0 the outer fluid (plasma) viscosity, v the interfacial velocity of membrane and A_i the membrane surface area of the ith RBC. The suspension shear viscosity μ^* is often expressed in terms of the viscosity μ_0 of the carrier fluid and a perturbation $\delta\mu$ (i.e. $\mu^* = \mu_0 + \delta\mu$), sometimes analytically obtained by truncating a perturbative approach at leading order (e.g. for small deformability or very dilute conditions). This leads to the introduction of the relative viscosity μ_{re} and specific viscosity μ_{sp} defined as

$$\mu_{re} = \frac{\mu^*}{\mu_0} = 1 + \mu_{sp}, \qquad (2.27)$$

$$\mu_{sp} = \frac{\delta\mu}{\mu_0} = \frac{\Sigma_{12}^{(p)}}{\mu_0\dot{\gamma}}. \qquad (2.28)$$

For example, in a dilute suspension of rigid spheres with a volume fraction ϕ, it is well known that the specific viscosity μ_{sp} can be given by a polynomial equation of the first order of ϕ, $\mu_{sp} = \eta\phi$ ($=2.5\phi$) (Einstein 1911), where the coefficient η ($=2.5$) is the intrinsic viscosity which is defined as $\eta = \mu_{sp}/\phi$.

The first and second normal stress differences, typically used to quantify the suspension viscoelastic behaviour, are defined as

$$\frac{N_1}{\mu_0\dot{\gamma}} = \frac{\Sigma_{11}^{(p)} - \Sigma_{22}^{(p)}}{\mu_0\dot{\gamma}}, \qquad (2.29)$$

$$\frac{N_2}{\mu_0\dot{\gamma}} = \frac{\Sigma_{22}^{(p)} - \Sigma_{33}^{(p)}}{\mu_0\dot{\gamma}}. \qquad (2.30)$$

The particle pressure (Jeffery, Morris & Brandy 1993), which is the isotropic stress that exists in the particle phase, is given by

$$\frac{\Pi_p}{\mu_0\dot{\gamma}} = -\frac{\mathrm{tr}\,\Sigma^{(p)}}{3\mu_0\dot{\gamma}}. \qquad (2.31)$$

The particle pressure is analogous to the osmotic pressure in a colloidal suspension caused by the hydrodynamic interactions among the suspended particles without Brownian motion, and has been previously quantified for suspensions of deformable capsules (Clausen *et al.* 2011; Reasor Jr *et al.* 2013; Gross *et al.* 2014). In the following section, we show the numerical results obtained with $\lambda = 5$, and compare with those obtained at other values of λ to quantify the effect on the bulk suspension rheology.

3. Results

3.1. *Behaviour of a single RBC*

First, we investigate the behaviour of a single RBC at small deformations. When the RBC is placed perpendicular to the shear direction ($\Psi_0 = \pi/2$), it keeps flipping along the vortex angle for low Ca ($=0.05$), with $\Psi \sim \pi/2$ and with $-\pi/2 < \theta < \pi/2$, the so-called tumbling motion (figure 1c; see the supplementary movie 1). On the other hand, an RBC initially randomly placed, i.e. $\Psi_0 = $ rand. (at least $\Psi_0 \neq 0$ or $\neq \pi/2$), tends to orient parallel to the shear plane, showing a wheel-like configuration with $\Psi = 0$ and $\theta \sim \pi/4$, the so-called rolling motion (figure 1c; see the supplementary movie 2). Our numerical results suggest that a free mode of the RBC at low Ca is the rolling motion. Our numerical results also show that the stable rolling RBC has higher intrinsic viscosity than the tumbling RBC (see figure 1d). Since the orientation angle θ of a single deformable spherical capsule converges to $\pi/4$ in shear flow as $Ca \to 0$ (Barthés-Biesel 1980; Barthés-Biesel & Sgaier 1985), the orientation angle θ of the rolling RBC also converges to $\theta \to \pi/4$. Jeffery (1922) investigated the motion of a single ellipsoid in simple shear flow in the Stokes flow regime, and hypothesized that 'The particle will tend to adopt that motion which, of all the motions possible under the approximated equations, corresponds to the least dissipation'. Taylor (1923) experimentally confirmed Jeffery's hypothesis by investigating the orbit of a prolate or oblate spheroid in a Couette flow at a very low Re. However, our numerical results of intrinsic viscosity η do not agree with Jeffery's hypothesis, i.e. maximum in η, while agreeing with previous numerical results of deformable biconcave capsules (Gross *et al.* 2014).

The effects of Ca on the stable mode and intrinsic viscosity are now investigated. At least for $Ca \leqslant 0.4$, RBCs initially oriented with $\Psi_0 = \pi/4$ converge their orientation angles to that obtained for RBCs with $\Psi_0 = 0$ as shown in figure 2(a), where the insets represent the stable configurations at each Ca. Note that the final orientation is not changed if the RBCs are initially oriented with $\pi/4 < \Psi_0 < \pi/2$. When Ca increases ($\geqslant 0.8$), the rolling motion becomes unstable. For instance, RBCs subjected to the highest Ca that we investigated (i.e. $Ca = 1.2$) fluctuate for $0 \leqslant \Psi \leqslant \pi/2$, showing a multilobe-like shape (Lanotte *et al.* 2016), while RBCs at $Ca = 0.8$ for $\Psi \sim 0$ show a tumbling stomatocyte-like shape (Mauer *et al.* 2018) (figure 2b; see the supplementary movie 3 for $Ca = 1.2$ and movie 4 for $Ca = 0.8$). Such complex deformed shapes of RBCs are qualitatively similar to those reported by Mauer *et al.* (2018), where their smoothed dissipative particle dynamics model of RBCs with $\lambda = 5$ shifts from rolling discocytes (similar to the inset in figure 2a for $Ca = 0.05$) to rolling/tumbling stomatocytes (similar to the inset in figure 2a for $Ca = 0.2$ or 0.4) and finally attaining multilobes (similar to the inset in figure 2a for $Ca = 0.8$ or 1.2) as the shear rate increases. Despite the different configurations, the intrinsic viscosity η for high Ca is similar as shown in figure 2(d), and hence the effect of the stable modes on the intrinsic viscosity η reduces for increasing Ca. According to figure 2(d), the result for $\Psi_\infty = 0$ demonstrates significantly more shear-thinning (Skovborg *et al.* 1966; Cokelet & Meiselman 1968; Chien 1970) than in the case of $\Psi_\infty = \pi/2$.

The effect of the viscosity ratio λ on the intrinsic viscosity η is quantified for each orientation (i.e. $\Psi_\infty = 0$ or $\pi/2$), and shown in figure 3(a), where the stable mode of $\Psi_\infty = 0$ exhibits higher shear-thinning than the case of $\Psi_\infty = \pi/2$ for all λ. To summarize, a phase diagram of stable modes of a single RBC based on the orientation angles is given in figure 3(b) as functions of the viscosity ratio λ and the logarithm of Ca, where all the results are obtained with the simulations started
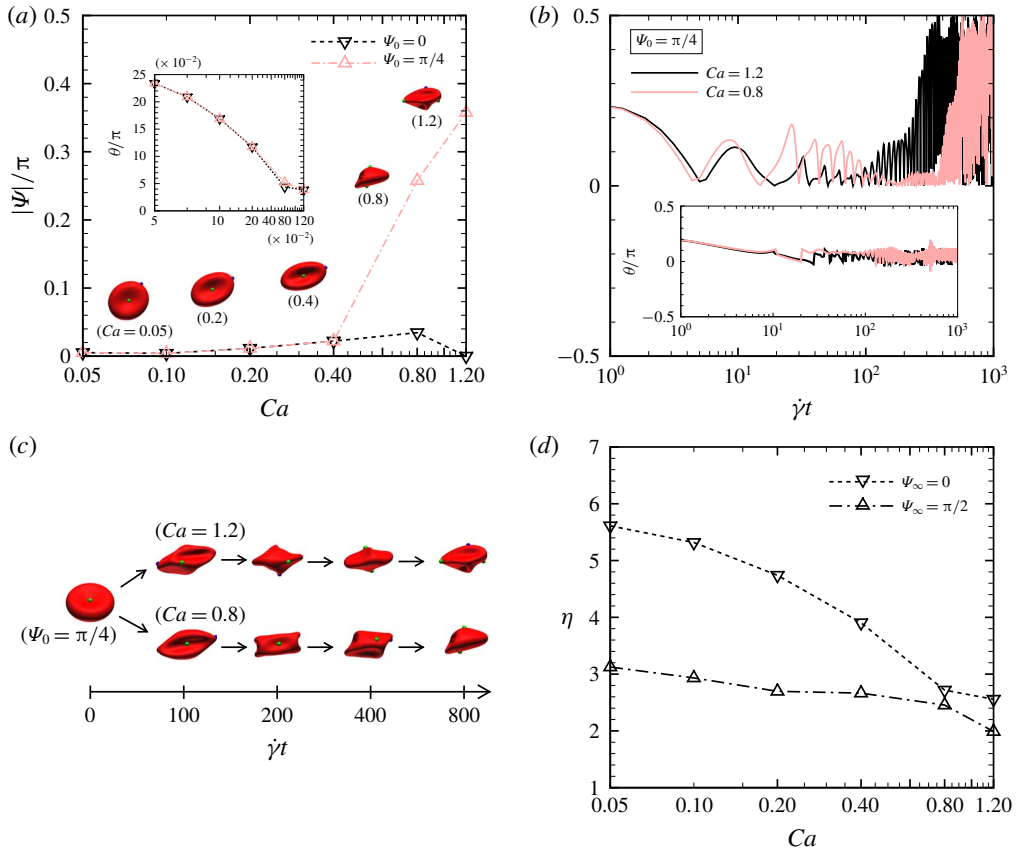
FIGURE 2. (Colour online) (*a*) Time average of the orientation angle θ and Ψ as a function of the logarithm of *Ca*. The simulations start from $\Psi_0 = 0$ (black inverse triangles) and $\Psi_0 = \pi/4$ (pale red triangles). Inset figures represent the stable configurations of the RBC with initial angle $\Psi_0 = \pi/4$ for each *Ca*. (*b*) Time history of the orientation angles θ and Ψ for $Ca = 0.8$ (pale red line) and $Ca = 1.2$ (black line), for initial angle $\Psi_0 = \pi/4$. (*c*) Snapshots of deformed RBCs at different times for $Ca = 0.8$ (lower) and $Ca = 1.2$ (upper). (*d*) Time average of the intrinsic viscosity η as a function of the logarithm of *Ca* for different stable modes, $\Psi_\infty = 0$ (inverse triangles) and $\Psi_\infty = \pi/2$ (triangles), obtained with the simulations started from $\Psi_0 = 0$ and $\Psi_0 = \pi/2$, respectively. These results are obtained with $\lambda = 5$.

with random orientations $\Psi_0 = rand$. For low *Ca*, most of the RBCs tend to show the rolling motion which corresponds to the rolling discocyte also reported by Mauer *et al.* (2018), but some of them show an unstable periodic rolling motion even after a long period of time; in other words, the orientation angles do not converge during the simulation time (at least $\dot{\gamma}t \leqslant 1000$). As an example, the supplementary movie 5 shows the result obtained with $\lambda = 0.1$ at $Ca = 0.2$. This periodic motion has been also called kayaking (oscillating–swinging) motion in previous numerical studies of biconcave capsules (Cordasco *et al.* 2014; Sinha & Graham 2015), similar to a classical Jeffery orbit (Jeffery 1922). For increasing *Ca*, most of the RBCs shift from the rolling to the swinging motion almost independently of λ (figure 3*b*). Based on several previous works on the dynamics of a single RBC, we define the swinging
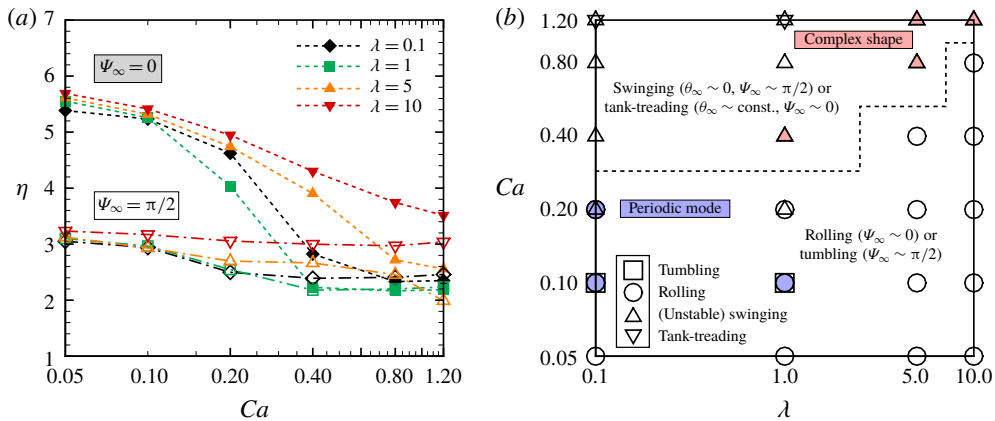
FIGURE 3. (Colour online) (*a*) Time average of the intrinsic viscosity η obtained with different viscosity ratios λ as a function of the logarithm of Ca for each stable mode: $\Psi_\infty = 0$ (dashed lines) and $\Psi_\infty = \pi/2$ (dash-dotted lines). The results for $\Psi_\infty = 0$ and $\Psi_\infty = \pi/2$ are obtained with initial orientation $\Psi_0 = 0$ and $\Psi_0 = \pi/2$, respectively. (*b*) Phase diagram of the stable modes of a single RBC as functions of the logarithm of λ and Ca, where the squares ($\square$) denote the tumbling motion, circles ($\bigcirc$) the rolling motion, triangles ($\triangle$) the unstable or stable swinging motion and inverse triangles ($\triangledown$) the tank-treading motion. The solid blue dots represent the periodic motions (see the supplementary movie 5) and the solid red triangles the complex shapes which demonstrate an unstable swinging motion. The dashed line separates the rolling motion from the (unstable) swinging motion. The results in (*b*) are obtained with random initial orientations.

motion when θ is periodic and $\Psi \neq 0$, while we define the tank-treading motion when θ is constant and $\Psi \sim 0$. In the swinging cases, especially for high viscosity ratios $\lambda \geqslant 5$ (figure 3*b*), RBCs tend to show complex shapes (or multilobes) as Ca increases. The stomatocyte, which can be assumed as one of the multilobe shapes, is found at $\lambda = 1$ for $Ca = 0.4$, which shifts to a stable swinging motion for higher Ca (figure 3*b*). Hence, these complex shapes can be assumed as a transient to the stable swinging motion, and we thus call its mode 'unstable swinging motion'. Sinha & Graham (2015) also showed that a biconcave capsule with $\lambda = 0.75$, with membrane following the SK law ($G_s = 2.5 \ \mu\text{N m}^{-1}$ and $C = 10$), transitions from the tumbling motion to the oscillating–swinging motion for $\dot\gamma \sim 465 \ \text{s}^{-1}$ and to the tank-treading motion for $\dot\gamma \sim 930 \ \text{s}^{-1}$ corresponding to $Ca \sim 1.12$. Mauer *et al.* (2018) showed that tank-treading RBCs can only be found for low λ ($\leqslant 3$) and high $\dot\gamma$ ($\geqslant 820 \ \text{s}^{-1}$), and that RBCs with $\lambda = 5$ subject to high shear rates are tumbling stomatocytes or multilobes. The phase diagram that we obtained is indeed consistent with these literature results (Sinha & Graham 2015; Mauer *et al.* 2018), since we also identify the tank-treading motion for $\lambda \leqslant 1$ and $Ca = 1.2$, and since RBCs with $\lambda \geqslant 5$ subject to high Ca exhibit multilobe shapes. More precise descriptions of the stable modes of single RBCs are needed to investigate the effect of the initial orientation angle Ψ_0, which is however beyond the scope of the present work. The dynamics of single RBCs has also been investigated in the past, e.g. in the studies by Omori *et al.* (2012), Cordasco *et al.* (2014), Sinha & Graham (2015) and Mauer *et al.* (2018).

3.2. *Behaviour of RBCs in semi-dilute and dense suspensions*

Next, individual RBCs in semi-dilute and dense suspensions are investigated, and examples of snapshots of the numerical results are shown in figure 4, where a
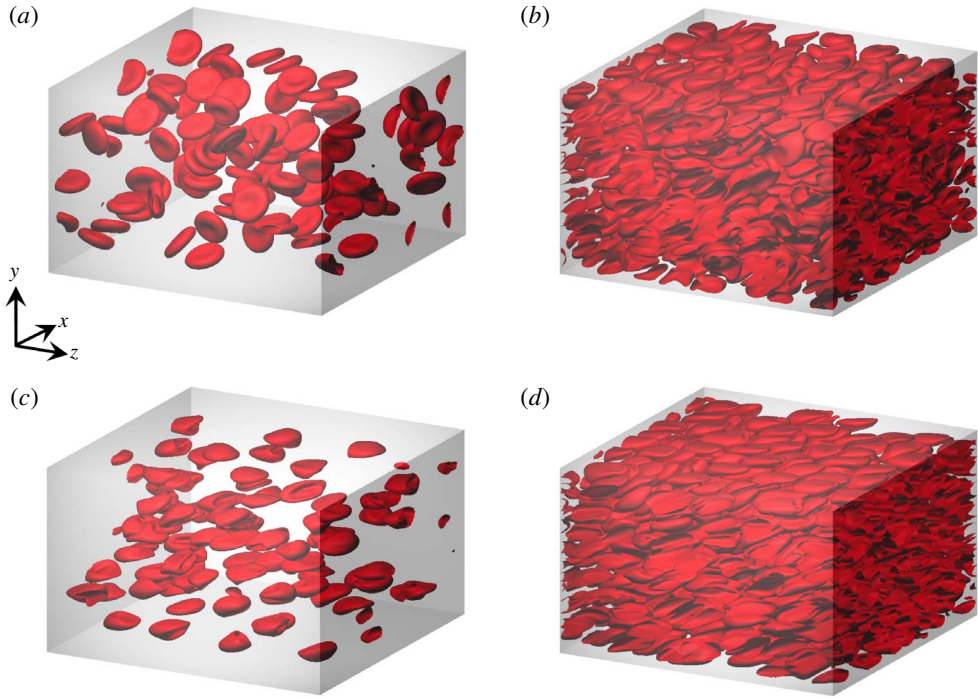
FIGURE 4. (Colour online) Snapshots of our numerical results for (*a,c*) semi-dilute suspensions ($\phi = 0.05$) and (*b,d*) dense suspensions ($\phi = 0.41$) with $\lambda = 5$. The results for $Ca = 0.05$ and 0.8 are reported in (*a,b*) and (*c,d*), respectively. The time evolutions of these snapshots are shown in the supplementary movies: movie 6 for (*a*), movie 7 for (*b*), movie 8 for (*c*) and movie 9 for (*d*).

semi-dilute suspension is defined for volume fraction $\phi = 0.05$, and a dense suspension for the highest ϕ that we investigated, i.e. $\phi = 0.41$. In semi-dilute suspensions, RBCs subjected to low $Ca = 0.05$ show small deformations, where both the rolling and tumbling motions coexist (figure 4*a*) (see the supplementary movie 6). In dense suspensions, however, due to the high packing, the RBCs are forced to exhibit only the swinging motion resulting in large elongations even for low $Ca = 0.05$ (figure 4*b*; see the supplementary movie 7). Indeed, as the volume fraction ϕ increases, the orientation angle Ψ immediately increases and saturates around $\Psi \sim 0.34\pi$, while the other orientation angle θ initially decreases and remains at $\theta \leqslant 0.1\pi$ as shown in figure 5(*a*), where the insets represent enlarged views of semi-dilute suspensions showing the coexistence of the rolling and tumbling motions, and of dense suspensions dominated by swinging motions. The different motions are well characterized in the time history of both orientation angles as shown in figures 5(*c*) and 5(*d*), respectively. These results clearly show that hydrodynamic interactions allow RBCs to shift from the rolling to the tumbling or swinging motions at different Ca from that for single RBCs. Since the tumbling and swinging motion is that which allows low intrinsic viscosity η as described above, hydrodynamic interactions decrease η in semi-dilute suspensions but enhance it for high volume fractions as shown in figure 5(*b*).

When Ca increases to 0.8, individual RBCs in semi-dilute suspensions deform largely and show complex shapes (figure 4*c*; see the supplementary movie 8).
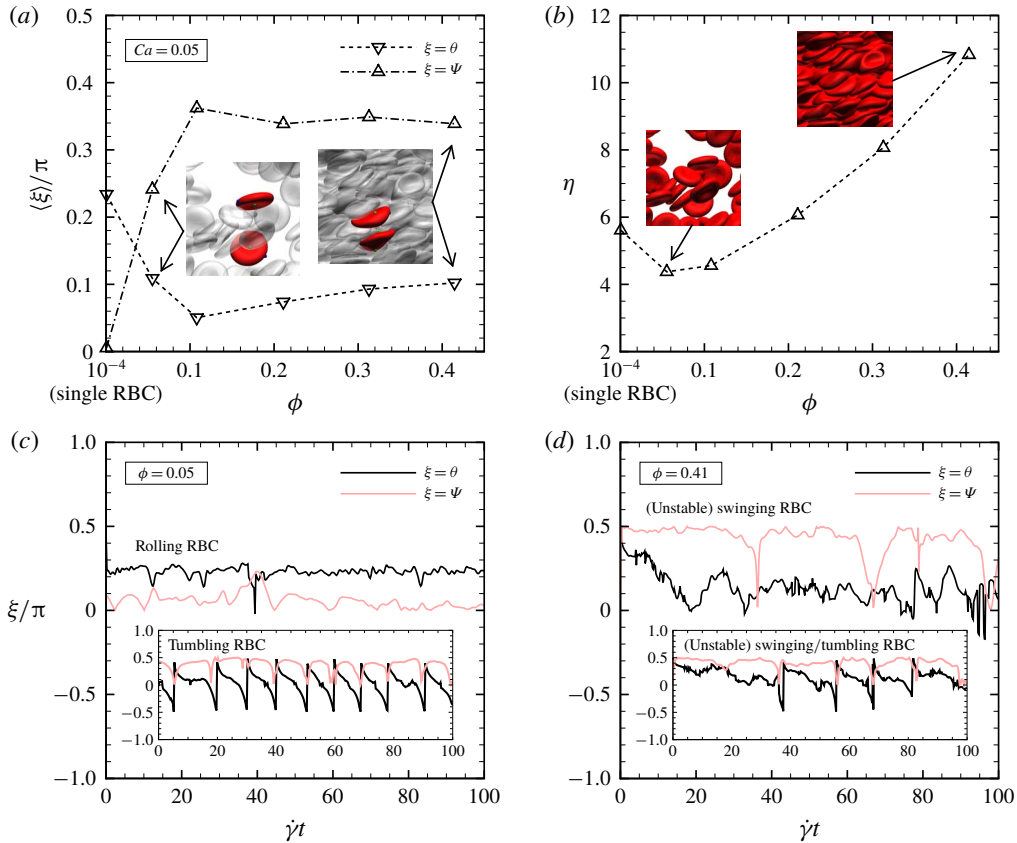
FIGURE 5. (Colour online) (*a*) Ensemble average of the orientation angles of RBCs for $Ca = 0.05$ and (*b*) the intrinsic viscosity η as a function of the volume fraction ϕ, where the insets are representative snapshots showing the coexistence of rolling and tumbling motions in a semi-dilute suspension and the unstable or stable swinging RBC in a dense suspension. These modes are identified by the time history of the orientation angles θ and Ψ for (*c*) semi-dilute and (*d*) dense suspensions. These results are obtained with $\lambda = 5$.

Since the deformation is induced by the hydrodynamic interactions, RBCs in dense suspensions elongate more than in the case with $Ca = 0.05$ (figure 4*d*; see the supplementary movie 9). Similarly to the case with $Ca = 0.05$, the orientation angle Ψ immediately increases as ϕ increases, but it slightly decreases from $\phi \sim 0.1$ onwards. Since RBCs subject to high Ca tend to show mostly swinging motions without multi-cellular interactions, the orientation angle θ is already small in the case of dilute suspensions (single RBC level), and slightly increases with ϕ as shown in figure 6(*a*), where the insets represent enlarged views of semi-dilute and dense suspensions showing the coexistence of the swinging and tank-treading motions. Here, we define the tank-treading motion as $\Psi \sim 0$ and $\theta \sim 0$ as in the previous numerical study by Omori *et al.* (2012). These are characterized in the time history by the two orientation angles reported in figure 6(*c*,*d*), where the swinging RBCs are the ones fluctuating in Ψ (i.e. $\Psi \neq \pi/2$). Since rolling motions do not exist for $Ca = 0.8$, the intrinsic viscosity does not much drop and it almost monotonically increases with ϕ as shown in figure 6(*b*), where the insets display instantaneous configurations.
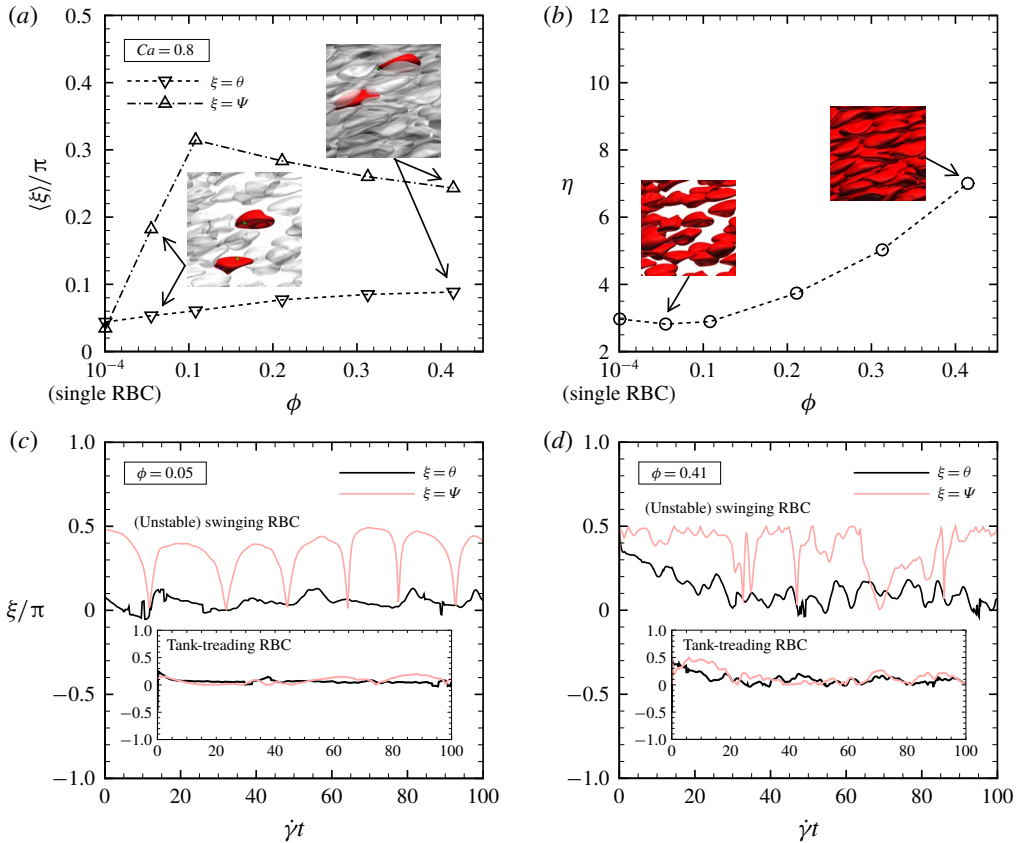
FIGURE 6. (Colour online) (*a*) Ensemble average of the orientation angles of RBCs for $Ca = 0.8$ and (*b*) the intrinsic viscosity η as a function of the volume fraction ϕ. Time history of the orientation angles for (*c*) semi-dilute and (*d*) dense suspensions. These results are obtained with $\lambda = 5$.

To summarize the results of stable modes of individual RBCs in dilute (single-cell level), semi-dilute ($\phi \sim 0.05$) and dense suspension ($\phi \sim 0.4$), we show the intrinsic viscosity η as a function of ϕ for different Ca in figure 7(*a*), where the drop of η in semi-dilute suspensions is commonly found at each Ca. The drop of η in semi-dilute suspensions is explained by the mode change from the rolling to tumbling motion, as reported in the phase diagram (figure 7*b*). On increasing ϕ, the probability of swinging RBCs increases resulting in the increase of η observed in figure 7(*a,b*). To see the relationship between the intrinsic viscosity of the suspension and the RBC deformation at high volume fractions, we show the deformation index d_{max}/d_{ref} in figure 7(*c*), where d_{max} and d_{ref} are the maximum distances between two points on the deformed and reference (i.e. without flow) membranes. We observe that d_{max}/d_{ref} increases similarly to η for relatively high volume fractions ($\phi > 0.05$), and hence high η can be associated with large deformation of swinging RBCs. The increase with ϕ is also found for the first normal stress difference $N_1/\phi\mu_0\dot{\gamma}$, while no significant differences are evident when varying Ca (figure 7*e*). Instead, the second normal stress difference $N_2/\phi\mu_0\dot{\gamma}$ decreases with ϕ, and again almost no difference is evident for different Ca (figure 7*f*). The particle pressure $\Pi_p/\phi\mu_0\dot{\gamma}$ also decreases with ϕ
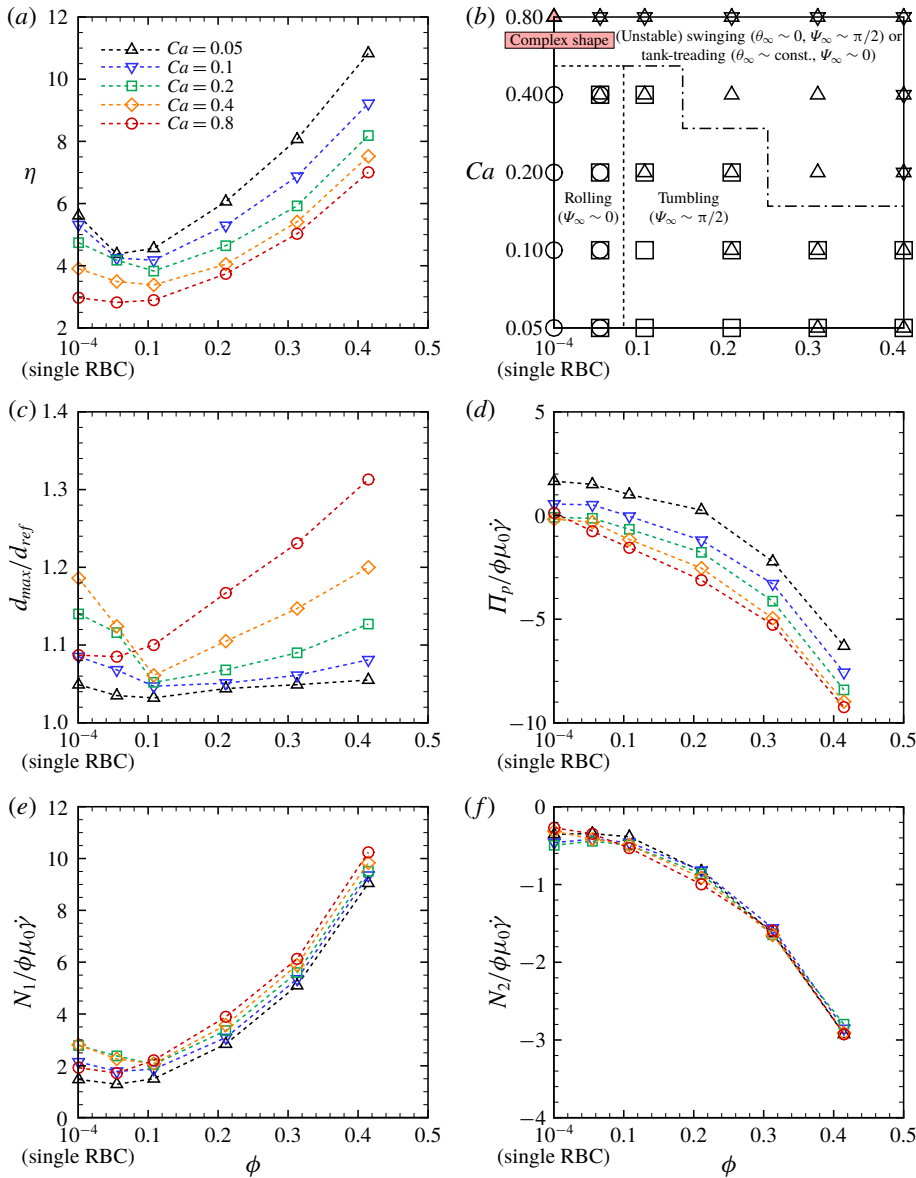
FIGURE 7. (Colour online) (*a*) The intrinsic viscosity η and (*b*) the phase diagram of the stable modes of RBCs as functions of ϕ and logarithm of Ca, where the squares (□) denote the tumbling motion, circles (○) the rolling motion, triangles (△) the unstable or stable swinging motion and inverse triangles (▽) the tank-treading motion. The red triangles denote the complex shape which demonstrates unstable swinging motions. The dashed line separates the rolling from the other motions, and the dash-dotted line the tumbling motions from the pure swinging/tank-treading motion. (*c*) The deformation index d_{max}/d_{ref}, where d_{max} and d_{ref} are the maximum distances between two points on the deformed and reference membranes (i.e. no flow condition), respectively. (*d*) The particle pressure $\Pi_p/\phi\mu_0\dot{\gamma}$ as a function of the volume fraction ϕ for different Ca. The (*e*) first and (*f*) second normal stress differences $N_i/\phi\mu_0\dot{\gamma}$ ($i = 1$ and 2, respectively). These results are obtained with $\lambda = 5$.

(figure 7*d*), similarly to the second normal stress difference (figure 7*f*), although the effect of *Ca* is more pronounced.

The effects of λ on the intrinsic viscosity η and on the stable mode are investigated at a fixed *Ca*, and the results are shown in figure 8. For low *Ca* (=0.05), the drop of η in semi-dilute suspensions ($\phi \sim 0.05$) is observed independently of the value of λ (figure 8*a*) because the mode changes from the rolling to the tumbling motion (figure 8*c*). For high *Ca* (=0.8), the mode change is not evident in semi-dilute suspensions (figure 8*d*), and hence the drop of η is not found for every λ (figure 8*b*). As shown in figure 8(*e*,*f*), the increase of η for relatively high volume fractions can also be explained by large deformations of swinging RBCs independently of λ.

4. Discussion

4.1. *Comparison with experiments*

Our numerical results for the relative viscosities μ_{re} in dense suspensions ($\phi = 0.41$) are compared with the previous experimental results of Chien (1970) and Cokelet & Meiselman (2007). In the study of Chien (1970), the viscosities of normal human RBC suspensions in heparinized plasma or in 11 % albumin–Ringer solution at 45 % volume fraction were measured in a coaxial cylinder viscometer at 37 °C, where the 11 % albumin–Ringer solution had the same viscosity as plasma (i.e. $\mu_0 = 1.2$ cP) but did not cause RBC aggregation. Cokelet & Meiselman (2007) also measured the viscosity of normal human RBC suspension in plasma at 40 % volume fraction. Therefore, these experimental conditions in RBC suspensions correspond to $\lambda = 5$. Indeed, our numerical results obtained with $\lambda = 5$ well agree with the experimental results, especially those of Cokelet & Meiselman (1968) as shown in figure 9(*a*).

Figure 9(*b*) shows the numerical results of μ_{re} as a function of ϕ for $\lambda = 5$. The relative viscosity μ_{re} for each *Ca* exponentially increases with ϕ, and μ_{re} tends to decrease as *Ca* increases. This behaviour is the same when the viscosity ratio changes (data not shown). Our numerical results for μ_{re} are compared with the empirical expression proposed by Krieger & Dougherty (1959):

$$\mu_{re} = \left(1 - \frac{\phi}{\phi_m}\right)^{-\eta\phi_m}, \qquad (4.1)$$

where ϕ_m is the maximum volume fraction. Although (4.1) was originally proposed for rigid-sphere suspensions, it allows us to estimate the viscosity for particles of any shape by choosing suitable ϕ_m and η, e.g. Tao & Huang (2011) set $\phi_m = 0.72$ and $\eta = 2.3$ in order to estimate the relative viscosity μ_{re} experimentally obtained in blood with the plasma viscosity ≈ 1.0 cP at 37 °C and the viscosity ratio λ around 5. Our numerical results agree well also with this empirical expression (4.1) with the same parameters proposed by Tao & Huang (2011), especially for high *Ca* (=0.8).

Figure 9(*c*) shows the numerical results for μ_{re} obtained with different λ for $Ca = 0.2$, which corresponds to a shear rate $\dot{\gamma} = 167$ s^{-1}, as a function of the volume fraction ϕ. These results are compared with previous measurements obtained with acetaldehyde-fixed human RBC suspension in plasma for $\dot{\gamma} = 170.8$ s^{-1} (Brooks *et al.* 1970), and also with normal human/sickle RBC suspension for $\dot{\gamma} > 100$ s^{-1} (Goldsmith 1972). Again, we confirm that our numerical results are well within those of normal and sickle RBCs. It is also known that cytoplasmic viscosity nonlinearly increases with haemoglobin concentration, resulting in alteration of the cell deformability. The usual distribution of haemoglobin concentration in individual RBCs
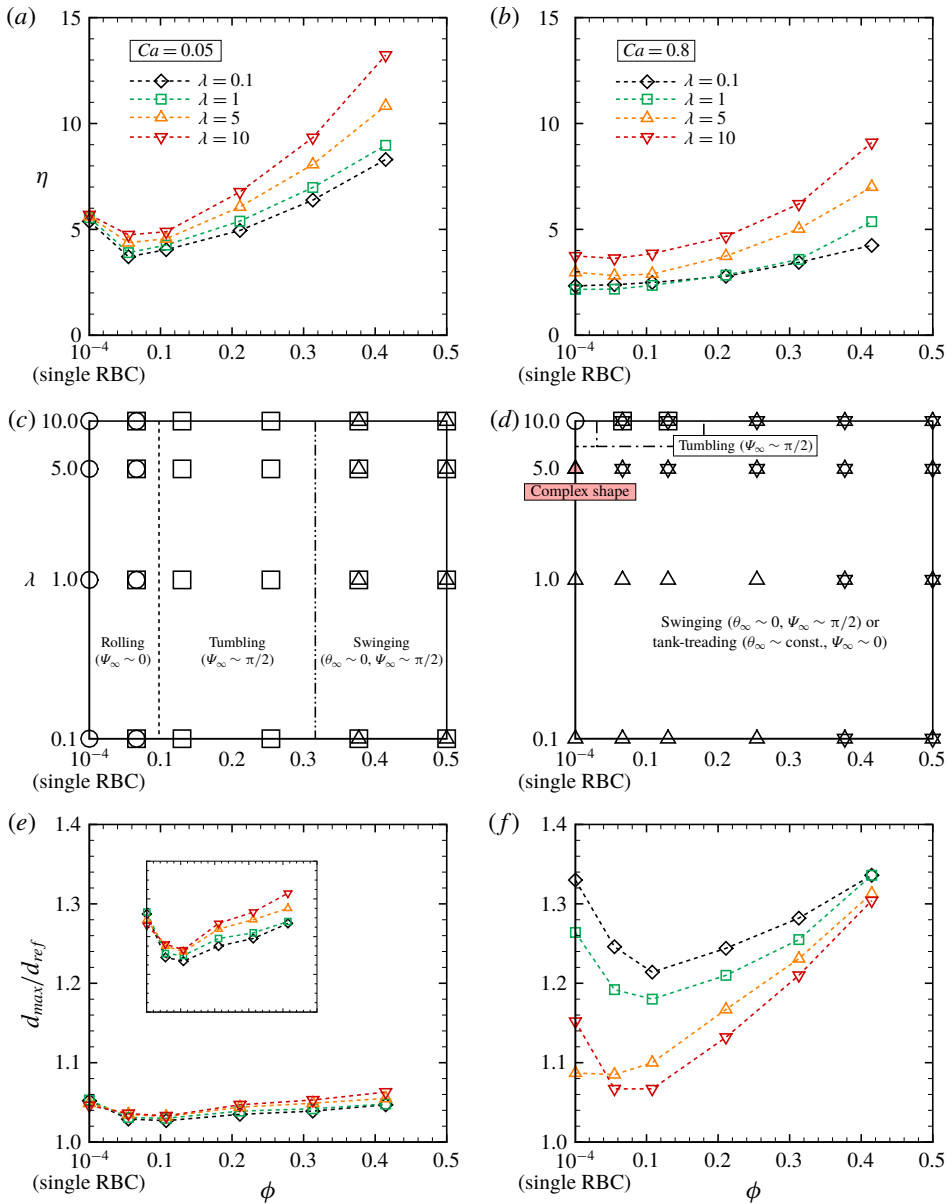
FIGURE 8. (Colour online) (*a,b*) The intrinsic viscosity η as a function of the volume fraction ϕ for (*a*) low $Ca = 0.05$ and (*b*) high $Ca = 0.8$. (*c,d*) The phase diagrams of the stable modes of RBCs as functions of ϕ and logarithm of λ for (*c*) $Ca = 0.05$ and (*d*) $Ca = 0.8$, where the squares (□) denote the tumbling motion, circles (○) the rolling motion, triangles (△) the unstable or stable swinging motion and inverse triangles (▽) the tank-treading motion. The solid red triangles denote the complex shapes which demonstrate unstable swinging motions. The dashed line in (*c*) separates the rolling motion from the tumbling motion, the dash-dotted line in (*c*) separates the pure tumbling motion from the swinging motion and the dash-dotted line in (*d*) separates the tumbling motion from the swinging/tank-treading motion. (*e,f*) The deformation index d_{max}/d_{ref} for (*e*) low $Ca = 0.05$ and (*f*) high $Ca = 0.8$.
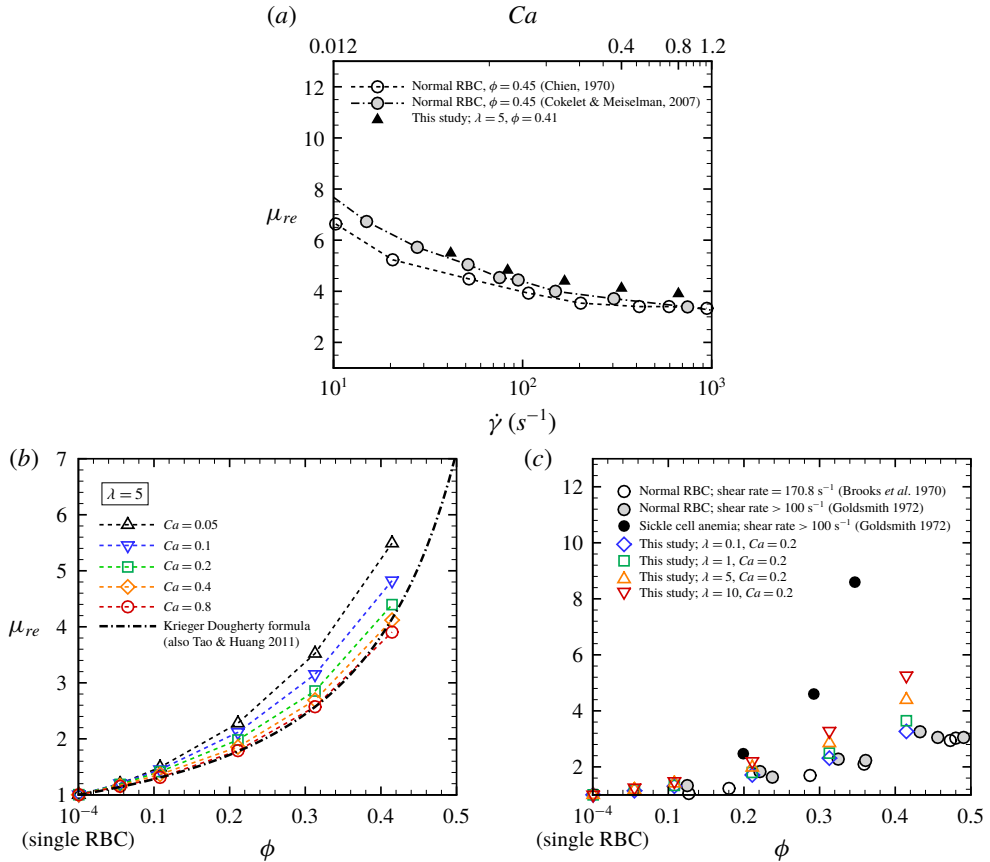
FIGURE 9. (Colour online) (*a*) Relative viscosity μ_{re} for $\phi = 0.41$ as a function of the logarithm of the shear rate $\dot{\gamma}$ obtained with $\lambda = 5$. The experimental results of normal human RBC suspension in plasma, 11 % albumin–Ringer solution for $\phi = 0.45$ at 37 °C (Chien 1970), and in plasma at $\phi = 0.4$ (Cokelet & Meiselman 2007) are also displayed as white and grey circles, respectively. The viscosity of 11 % albumin–Ringer solution is the same as that of plasma, i.e. $\mu_0 = 1.2$ cP. (*b*) Relative viscosity μ_{re} obtained with $\lambda = 5$ as a function of the volume fraction ϕ for different *Ca*. The empirical expression reported in (4.1) with the parameters proposed by Tao & Huang (2011) is also displayed as a dash-dotted line. (*c*) Relative viscosity μ_{re} as a function of volume fraction ϕ for different viscosity ratios λ at $Ca = 0.2$ ($\dot{\gamma} = 167$ s^{-1}). The experimental results of a suspension of acetaldehyde-fixed human RBCs in plasma for $\dot{\gamma} = 170.8$ s^{-1} are also displayed as white circles (Brooks, Goodwin & Seaman 1970). Moreover, the experimental data of suspensions of normal and sickle human RBCs for $\dot{\gamma} > 100$ s^{-1} are also displayed as black and grey circles, respectively (Goldsmith 1972).

ranges from 27 to 37 g dl^{-1} corresponding to the internal fluid viscosity (μ_1) being 5–15 cP (Mohandas & Gallagher 2008). The physiologically relevant viscosity ratio therefore can be taken as $\lambda = 4.2$–12.5 if the plasma viscosity is set to $\mu_0 = 1.2$ cP. In the case of sickle cell anaemia, on the other hand, the haemoglobin concentration is abnormal, e.g. the mean corpuscular haemoglobin concentration of sickle cells is potentially elevated to 44.4–47.6 g dl^{-1} (Evans *et al.* 1984). Since previous studies have shown that the viscosity of haemoglobin solution abruptly increases to 45 cP at

40 g dl^{-1}, up to 170 cP at 45 g dl^{-1} and 650 cP at 50 g dl^{-1} (Cokelet & Meiselman 1968; Mohandas & Gallagher 2008), sickle cells with haemoglobin concentration of 45 g dl^{-1} may have high cytoplasmic viscosity $\mu_1 \approx 170$ cP, where the viscosity ratio is taken as $\lambda \approx 140$ if physiological plasma viscosity ($\mu_0 = 1.2$ cP) is considered. Although the exact haemoglobin concentration is different depending on the type of sickle cell disease and on the person, the relative viscosity μ_{re} of blood with sickle cell anaemia should be higher at any shear rates than that of normal blood (Chien *et al.* 1970; Usami *et al.* 1975; Kaul & Xue 1991).

4.2. *Comparison with other numerical models*

Next, we compare our numerical results of stresslet with those obtained with other membrane constitutive models: the spectrin-link model (Reasor Jr *et al.* 2013) and the continuum-based capsule model (Gross *et al.* 2014) whose membrane follows SK law but with repulsive forces between the RBCs. For reasonable comparison, we define the effective capillary number as $Ca_{eff} = \mu_{re}Ca$. Note that the definition of Ca in those previous works (Reasor Jr *et al.* 2013; Gross *et al.* 2014) is the same as used here and reported in (2.1). Figure 10(*a*) shows the intrinsic viscosity η as a function of Ca_{eff}. Independently of the numerical model used, the RBC suspensions show a shear-thinning behaviour; however, our results exhibit higher intrinsic viscosity than in the other two studies. While η in our results decreases for all Ca_{eff} as the viscosity ratio decreases from $\lambda = 5$ to $\lambda = 1$, in the previous studies η was almost independent of the value of λ (figure 10*a*). Although the results of Reasor Jr *et al.* (2013) and Gross *et al.* (2014) exhibit similar η, the particle pressure $\Pi_p/\mu_0\dot{\gamma}$ (figure 10*b*) and the two normal stress differences $N_i/\mu_0\dot{\gamma}$ (figure 10*c,d*) are quite different between the two previous studies. We think that the discrepancies among the three numerical studies of the stresslet values shown in figure 10 are mainly due to the difference in the choice of constitutive model for the RBC membrane, the contact model between RBCs and the boundary conditions. Comparing the results of the present study with those of Reasor Jr *et al.* (2013), we conclude that the stresslet is sensitive to the membrane constitutive model. Although the membrane model applied in Gross *et al.* (2014) and that of the present study are the same, Gross *et al.* (2014) considered repulsive forces between the RBCs. Such a contact model guarantees a certain amount of fluid between the RBCs, which is likely to decrease the relative viscosity (S_{12}) of the RBC suspension and also affect the other components of the particle stresslet tensor (S_{ij}). The different boundary conditions are also likely to partially affect the stresslet. Reasor Jr *et al.* (2013) used the Lees–Edwards boundary condition (Lees & Edwards 1972) to consider an unbounded shear flow, while Gross *et al.* (2014) and the present study consider a wall-bounded shear flow. However, we believe that the effect of a solid wall on the solution is limited because our numerical results (e.g. μ_{sp} and $N_i/\mu\dot{\gamma}$) for suspensions of spherical particles in a bounded shear flow agree well with those of the previous numerical studies of Matsunaga *et al.* (2016), where an unbounded shear flow was solved by the boundary-element method (see figure 13). These results suggest that the stresslet will be independent of numerical methods if the same membrane constitutive model and contact model between particles are used, and also indicate that the domain size used here is adequate. Gross *et al.* (2014) systematically investigated the stresslet for relatively low Ca_{eff} ($10^{-4} \leqslant Ca_{eff} \leqslant 10^{-1}$) at $\lambda = 1$. Our numerical results provide insight into stresslet for relatively high Ca_{eff} ($10^{-1} \leqslant Ca_{eff} \leqslant 1$), which correspond to venule and arteriole environments in humans. Although the particle pressure and normal stress differences are difficult to measure in experiments, we hope that our numerical results will stimulate not only numerical but also experimental studies to clearly show the viscoelastic behaviour of blood.
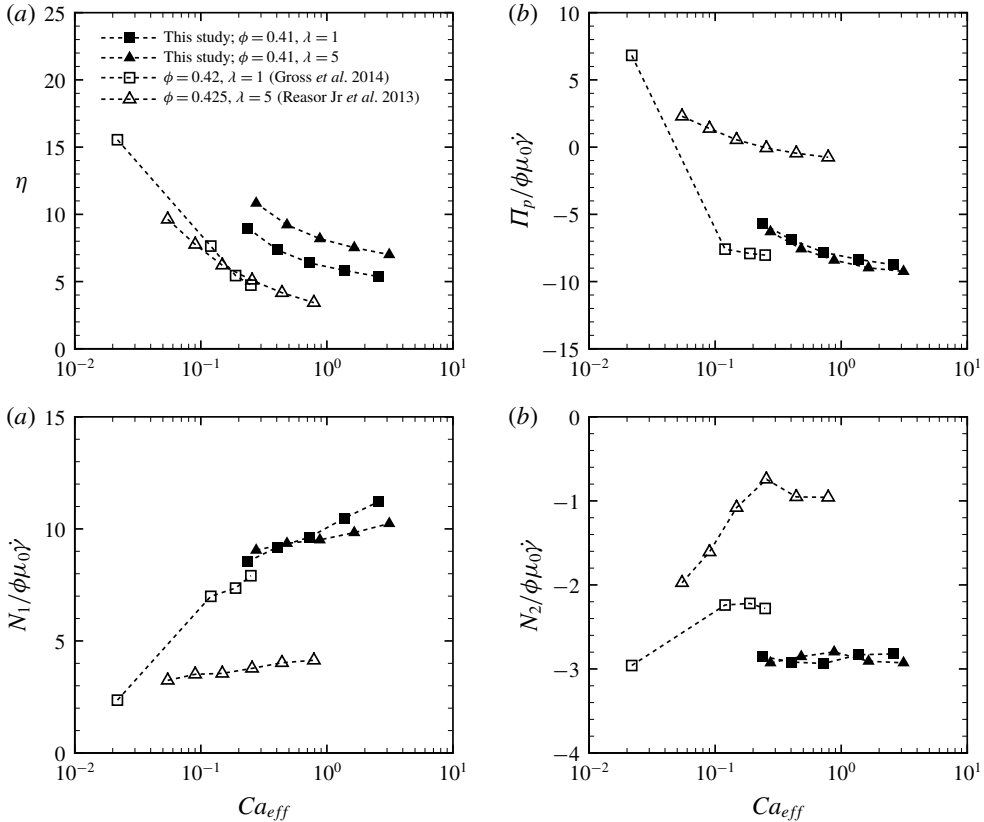
FIGURE 10. (*a*) The intrinsic viscosity η, (*b*) the particle pressure $\Pi_p/\mu_0\dot{\gamma}$ and the (*c*) first and (*d*) second normal stress differences $N_i/\mu_0\dot{\gamma}$ ($i = 1$ and 2) for $\phi = 0.41$ as a function of the effective capillary number Ca_{eff}. The previous numerical results for $\lambda = 1$ ($\phi = 0.42$) by Gross *et al.* (2014) and $\lambda = 5$ ($\phi = 0.425$, $k_b = 2.4 \times 10^{-19}$ J) by Reasor Jr *et al.* (2013) are also displayed for comparison.

4.3. *Effective volume fraction*

Conventionally, the relative viscosity μ_{re} ($= 1 + \mu_{sp}$) of dilute and semi-dilute particulate suspensions can be described by a polynomial expression in the volume fraction ϕ (Einstein 1911; Taylor 1932; Stickel & Powell 2005). For example, Einstein (1911) proposed for dilute suspensions of rigid particles that $\mu_{re} = 1 + 2.5\phi$, while Taylor (1932) proposed a modified law for particles including an internal fluid: $\mu_{re} = 1 + 2.5\tilde{\lambda}\phi$, where $\tilde{\lambda}$ is Taylor's factor defined as $\tilde{\lambda} = (\lambda + 0.4)/(\lambda + 1)$. However, our numerical results show that the intrinsic viscosity η ($= \mu_{sp}/\phi$) of RBC suspensions is not constant but first decreases from dilute to semi-dilute suspensions because of the mode change of RBCs from rolling to tumbling. This suggests that a simple polynomial approach cannot be applied to RBC suspensions even for low volume fractions; this issue cannot be solved by any higher-order expansions, since they necessarily involve particle–particle interactions and thus any higher-order coefficients would depend on the local flow and/or on the local microstructure. For high volume fractions, an exponential expression may be applicable. Rosti & Brandt (2018) proposed that the effective volume fraction ϕ_e, which is a collective
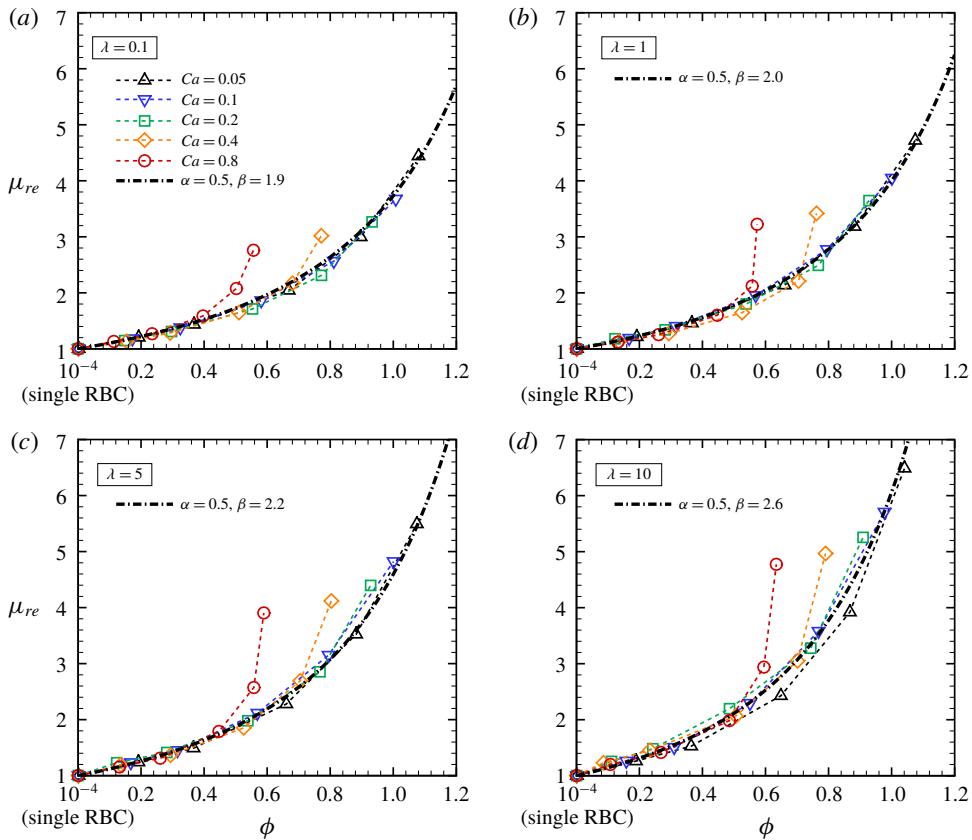
FIGURE 11. (Colour online) Relative viscosity μ_{re} as a function of the effective volume fraction ϕ_e for different Ca at each specific viscosity ratio: (*a*) $\lambda = 0.1$, (*b*) $\lambda = 1$, (*c*) $\lambda = 5$ and (*d*) $\lambda = 10$. The dash-dotted lines are exponential curves defined as $\mu_{re} = (1 - \alpha \phi_e)^{-\beta}$ with $\alpha = 0.5$ and $\beta|_{\lambda=0.1} = 1.9$, $\beta|_{\lambda=1} = 2.0$, $\beta|_{\lambda=5} = 2.2$ and $\beta|_{\lambda=10} = 2.6$.

volume fraction of spheres whose radius is defined with the semi-minor axis a_2 (here, $a_1 \geqslant a_3 \geqslant a_2$) of deformed spherical particles, is able to describe the relative viscosity of suspensions of deformable particles. Here, we define the effective volume fraction ϕ_e with the semi-middle axis a_3 of a deformed RBC, i.e. $\phi_e = N^R 4\pi a_3^3/(3V)$, where N^R is the number of RBCs in the computational box of volume V. The length of the semi-middle axis a_3 of the deformed RBC is obtained from the eigenvalues of the inertia tensor of an equivalent ellipsoid approximating the deformed RBC (Ramanujan & Pozrikidis 1998). Figure 11 shows the relative viscosity μ_{re} as a function of the effective volume fraction ϕ_e: for each λ, the numerical results for μ_{re} successfully collapse on a single nonlinear master curve, except for the case with high $Ca \geqslant 0.4$, where the fit works only in the case of low/moderate volume fraction, and fails in the case of a fully dense suspension. The fail of the fit for high Ca and ϕ is limited to the cases of RBCs showing complex shapes, e.g. multilobes. Indeed, in these cases the shape is mostly asymmetric and its approximation with an equivalent ellipsoid is not reliable. The single nonlinear curves are fitted by a general exponential expression:

$$\mu_{re} = (1 - \alpha \phi_e)^{-\beta}, \qquad (4.2)$$

where $\alpha = 0.5$ and $\beta|_{\lambda=0.1} = 1.9$, $\beta|_{\lambda=1} = 2.0$, $\beta|_{\lambda=5} = 2.2$ and $\beta|_{\lambda=10} = 2.6$. The coefficients α and β in (4.2) are related to those in the Krieger–Dougherty formula (4.1) by the following relations: $\alpha = 1/\phi_m$ and $\beta = -\eta\phi_m$; Tao & Huang (2011) proposed the following values for the coefficients: $\phi_m = 0.72$ and $\eta = 2.3$. Gross *et al.* (2014) proposed a toy model based on the effective medium theory by considering the effects of Ca and higher volume fraction ϕ, but up to now no model has been able to fully predict the behaviour of the relative viscosity. The next challenge may be constructing a model that is able to cover a wide range of viscosity ratios and large deformation of RBCs.

5. Conclusion

We numerically investigate the rheology of a suspension of RBCs in a wall-bounded shear flow for a wide range of volume fractions ϕ, viscosity ratios λ and capillary numbers Ca assuming the Stokes flow regime. The RBCs are modelled as biconcave capsules, whose membrane follows the SK constitutive law. The problem is solved numerically through GPU computing, using the LBM for the inner and outer fluid and the FEM to follow the deformation of the RBC membranes.

A single RBC subjected to low Ca tends to orient to the shear plane and exhibits rolling motion as a stable mode associated with higher intrinsic viscosity η ($=\mu_{sp}/\phi$) than tumbling motion. As Ca increases, the mode shifts from rolling to swinging motion, and the intrinsic viscosity η decreases. Hydrodynamic interactions (higher volume fraction) also allow RBCs to exhibit the tumbling or swinging motions resulting in a decrease of the intrinsic viscosity η for dilute and semi-dilute suspensions. This suggests that a simple polynomial equation of the volume fraction ϕ for the relative viscosity μ_{re} ($=1 + \mu_{sp}$) cannot be applied to RBC suspensions at low volume fractions. The relative viscosity μ_{re} for high volume fractions, however, can be well described as a function of an effective volume fraction ϕ_e, defined by the volume of spheres of radius equal to the semi-middle axis of the deformed RBC. For all λ considered, the relative viscosity μ_{re} successfully collapses on a single nonlinear curve as a function of ϕ_e except for the case with $Ca \geqslant 0.4$, where the fit works only in the case of low/moderate volume fractions.

We hope that our numerical results will stimulate the numerical and experimental study of haemorheology, aiming to gain insight not only into suspension rheology but also into the precise diagnosis of patients with haematologic disorders.

Acknowledgements

Supplementary movies

Supplementary movies are available at https://doi.org/10.1017/jfm.2019.393.

Appendix A. Numerical set-up

A.1. *Behaviour of a single capsule and RBC with different viscosity ratios*

To validate our numerical approach to update the viscosity in the fluid lattice, we tested the deformation of a single spherical capsule for different Ca and different viscosity ratios λ ($=0.2$, 1, 5 and 10). The capsule deformation is quantified by the Taylor parameter D_{12}, which is defined as

$$D_{12} = \frac{|a_1 - a_2|}{a_1 + a_2}, \tag{A 1}$$

where a_1 and a_2 are the lengths of the semi-major and semi-minor axes of the deformed capsule (or RBC), and are obtained from the eigenvalues of the inertia tensor of an equivalent ellipsoid approximating the deformed capsule (Ramanujan & Pozrikidis 1998). Time average starts after the non-dimensional time $\dot{\gamma}t = 40$ to reduce the influence of the initial conditions, and continues to $\dot{\gamma}t = 100$. Our numerical results are compared with previous numerical results obtained with the BIM (Foessel *et al.* 2011). The resolutions of the fluid and membrane meshes are the same as in the analysis above. For reasonable comparison with previous numerical study (Foessel *et al.* 2011), the same parameters are considered and the membrane is modelled with the SK constitutive law (2.6) with the area dilation modulus $C = 1$ and without bending resistance. Figure 12(*a*) shows that our numerical results are in good agreement with those of Foessel *et al.* (2011).

To characterize the surface shear elastic modulus G_s for RBCs, we performed a numerical simulation reproducing the stretching of RBCs by optical tweezers (Suresh *et al.* 2005); see figure 12(*b*). An RBC membrane with $G_s = 4$ µN m^{-1}, $C = 10^2$ and $k_b = 5 \times 10^{-19}$ J is laterally stretched by applying constant forces to two points of the membrane surface of radius equal to 1 µm. Modulus G_s is thus obtained to capture the nonlinear deformation curve obtained from the experiment. Using these parameters, we also tested the behaviour of a single RBC, and compare the normal stress differences $N_i/\phi\mu_0\dot{\gamma}$ ($i = 1$ and 2) with those of previous numerical results obtained with the BIM (Omori *et al.* 2014) in figure 12(*c*). Again, our numerical results are in good agreement with those of the literature, although the value of $N_1/\phi\mu_0\dot{\gamma}$ obtained with $\lambda = 3$ and Ca ($=1$) is slightly larger than that of the BIM.

A.2. *Effect of the domain size*

We have tested the computational domain size, especially the wall-to-wall distance H, and investigated its effect on the suspension behaviour. Although the influence of H upon particle shear stress and relative viscosity was systematically investigated by Krüger, Varnik & Raabe (2011), and the same computational domain size as in our study has been successfully applied to previous numerical studies of particle suspensions (Picano *et al.* 2013; Rosti & Brandt 2018), we also tested several parameters of deformed RBCs for different domain heights H ($=7.5a$, $12.5a$ and $15a$). The results of each parameter reported in table 1 are compared with those of the reference domain height $H = 10a$; in particular, we have analysed the ensemble average of the Taylor parameter $\langle D_{12} \rangle$, the orientation angle $\langle \theta \rangle$, the specific viscosity μ_{sp}, the particle pressure $\Pi_p/\mu_0\dot{\gamma}$ and the normal stress difference $N_i/\mu_0\dot{\gamma}$ ($i = 1$ and 2). Here, the ensemble average of a parameter $\langle \chi \rangle$ is defined as

$$\langle \chi \rangle = \frac{1}{MN} \sum_m^M \sum_n^N \chi^{m,n}, \tag{A 2}$$
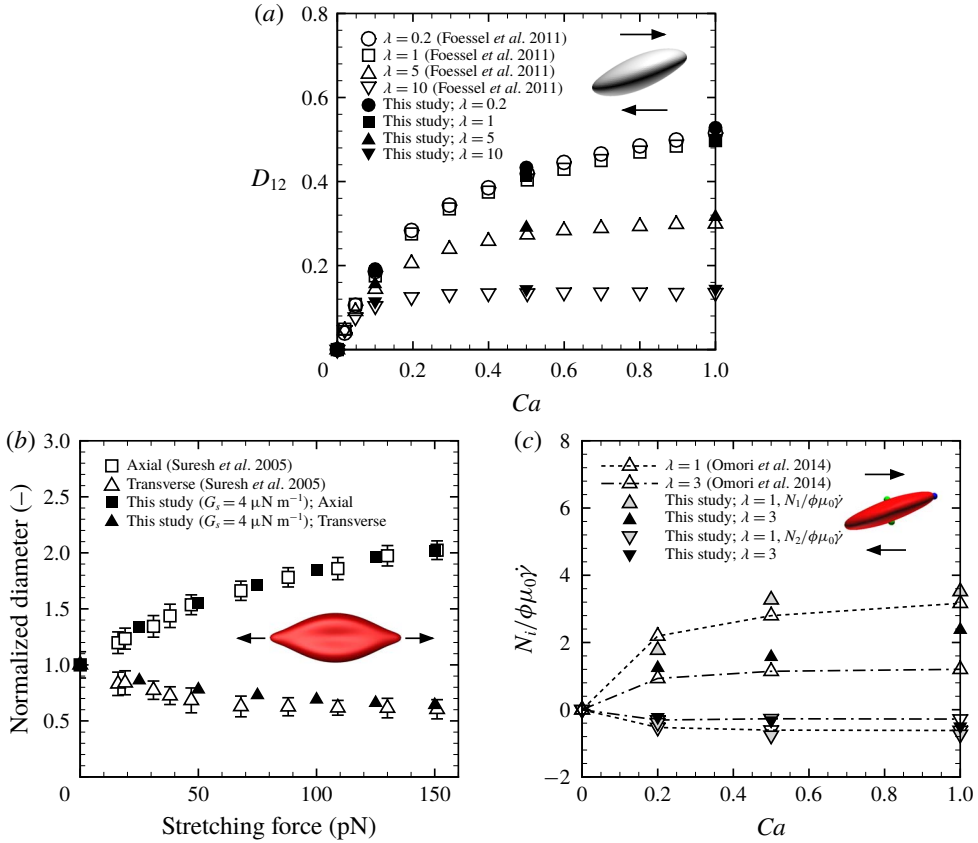
FIGURE 12. (Colour online) (*a*) Time-averaged Taylor parameter D_{12} of an SK spherical capsule as a function of *Ca* for different viscosity ratios λ (=0.2, 1, 5, and 10); previous numerical results of Foessel *et al.* (2011) are also displayed. The inset represents a tank-treading spherical capsule at $Ca = 1.0$ and $\lambda = 1$. (*b*) Comparison of the deformation of an RBC stretched by optical tweezers in an experiment (Suresh *et al.* 2005) and in our numerical simulation: an RBC membrane with $G_s = 4\ \mu\text{N m}^{-1}$, $C = 10^2$ and $k_b = 5 \times 10^{-19}$ J is laterally stretched by applying constant forces to two points of the membrane surface of radius equal to 1 μm. The inset represents the RBC stretched by 100 pN forces. (*c*) Time-averaged normal stress difference $N_i/\phi\mu_0\dot{\gamma}$ (*i* = 1 and 2) for $\lambda = 1$ and 3; previous numerical results of Omori *et al.* (2014) are also displayed. The inset represents a tank-treading RBC at $Ca = 1.0$ and $\lambda = 1$.

where *M* and *N* are the number of time steps and capsules, respectively. The error for each observable is defined by

$$\varepsilon_\chi = \left| \frac{\langle \chi \rangle - \langle \chi^{ref} \rangle}{\langle \chi^{ref} \rangle} \right|, \tag{A 3}$$

where the superscript *ref* indicates the reference values. The results of each parameter and the corresponding relative errors are listed in table 1. Since differences between the case with the largest height ($H = 12.5a$) and our reference case are less than 5 % in the orientation angle and 3 % in the others, the results presented in this study are all obtained with the domain height of $H = 10a$.

Height H	7.5a	10a (reference)	12.5a
Number of RBCs	258	344	442
$\langle D_{12} \rangle$	0.51130	0.50960	0.50700
$\varepsilon_{D_{12}}$	0.00334	—	0.00510
$\langle \theta \rangle / \pi$	0.08005	0.07835	0.07684
ε_{θ}	0.04932	—	0.04949
μ_{sp}	0.86880	0.85440	0.88010
$\varepsilon_{\mu_{sp}}$	0.01685	—	0.03008
$\Pi_p / \mu_0 \dot{\gamma}$	-0.58130	-0.53580	-0.52560
ε_{Π_p}	0.08492	—	0.01904
$N_1 / \mu_0 \dot{\gamma}$	0.80310	0.75340	0.75790
ε_{N_1}	0.06597	—	0.00597
$N_2 / \mu_0 \dot{\gamma}$	-0.21390	-0.19250	-0.18940
ε_{N_2}	0.11117	—	0.01610

TABLE 1. Effect of domain height H on the ensemble average of the Taylor parameter $\langle D_{12} \rangle$, the orientation angle $\langle \theta \rangle$, the specific viscosity μ_{sp}, the particle pressure $\Pi_p / \mu_0 \dot{\gamma}$ and the normal stress difference $N_i / \mu_0 \dot{\gamma}$ ($i = 1$ and 2). The error of each parameter ε_χ is defined by (A 3). The simulations were performed at $\phi = 0.21$, $Ca = 0.4$ and $\lambda = 5$.

A.3. *Suspension of spherical capsules*

We simulate suspensions of neo-Hookean (NH) spherical capsules for different Ca and $\phi = (0.12, 0.24$ and $0.35)$, as reference for the results pertaining to RBCs and to further validate our numerical model. The NH constitutive law is given as

$$w_s^{NH} = \frac{G_s}{2} \left(I_1 - 1 + \frac{1}{I_2 + 1} \right). \tag{A 4}$$

The viscosity ratio is set to be $\lambda = 1$, and the bending modulus is the same as that of the model of RBCs in this study, i.e. $k_b = 5 \times 10^{-19}$ J. Our numerical results are compared with previous numerical results of NH spherical capsules simulated by the BIM in an unbounded domain obtained by Matsunaga *et al.* (2016).

Figure 13(*a*) shows the snapshots of our numerical results for different ϕ. The ensemble averages of the Taylor parameter $\langle D_{12} \rangle$ and of the orientation angle $\langle \theta \rangle$ of the NH spherical capsules as a function of the volume fraction ϕ are also shown in figure 13: the values of $\langle D_{12} \rangle$ increase with the volume fraction (figure 13*b*), while the orientation angle decreases with it (figure 13*c*). Both these quantities are in good agreement with the results from the literature (Matsunaga *et al.* 2016). Time averages of the specific viscosity μ_{sp} and of the normal stress differences N_i ($i = 1$ and 2) are also compared with those reported by Matsunaga *et al.* (2016), and depicted in figures 13(*d*) and 13(*e*), respectively. The suspension viscosity increases with the particle volume fraction, as the absolute value of the normal stress difference, being the first positive and the second negative. In our simulations, a small bending resistance ($k_b = 5.0 \times 10^{-19}$ J) is considered to avoid the membrane buckling. Since our numerical results are in very good agreement with those of the previous study of Matsunaga *et al.* (2016), and quantitatively similar to those obtained in a larger domain (§ A.2), we will continue to use the rectangular box that is considered as reference in § A.2 and include a weak bending stiffness.
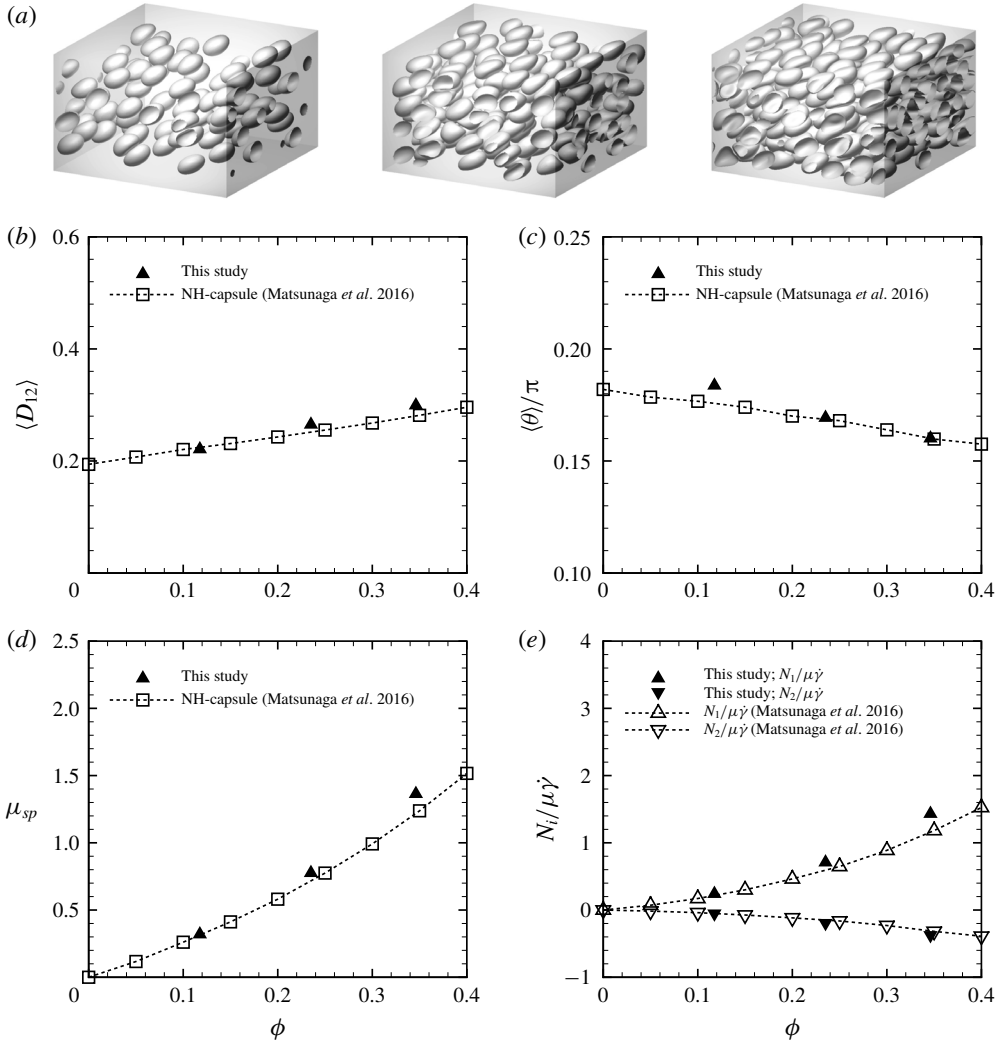
FIGURE 13. (a) Snapshots of numerical results of a suspension of NH spherical capsules for different volume fractions $\phi = 0.12$ (left), $\phi = 0.24$ (middle) and $\phi = 0.35$ (right). Ensemble average of (b) Taylor parameter $\langle D_{12} \rangle$, (c) orientation angle $\langle \theta \rangle / \pi$, (d) specific viscosity μ_{sp} and (e) first and second normal stress differences $N_i / \mu_0 \dot{\gamma}$ ($i = 1$ and 2) of NH spherical capsules, with viscosity ratio $\lambda = 1$, subjected to $Ca = 0.1$ as a function of the volume fraction ϕ. Our numerical results obtained with $\lambda = 1$ are compared with those reported in a previous numerical study of Matsunaga *et al.* (2016).

REFERENCES

ABKARIAN, M., FAIVRE, M. & VIALLAT, A. 2007 Swinging of red blood cells under shear flow. *Phys. Rev. Lett.* **98**, 188302.

BARTHÉS-BIESEL, D. 1980 Motion of a spherical microcapsule freely suspended in a linear shear flow. *J. Fluid. Mech.* **100**, 831–853.

BARTHÉS-BIESEL, D. & SGAIER, H. 1985 Role of membrane viscosity in the orientation and deformation of a spherical capsule suspended in shear flow. *J. Fluid. Mech.* **160**, 119–135.

BATCHELOR, G. K. 1970 The stress system in a suspension of force-free particles. *J. Fluid Mech.* **41**, 545–570.

BHATNAGAR, P. L., GROSS, E. P. & KROOK, M. 1954 A model for collision processes in gases. I. Small amplitude processes in charged and neutral one-component systems. *Phys. Rev.* **94**, 511–525.

BROOKS, D. E., GOODWIN, J. W. & SEAMAN, G. V. 1970 Interactions among erythrocytes under shear. *J. Appl. Physiol.* **28**, 172–177.

CHEN, S. & DOOLEN, G. D. 1998 Lattice Boltzmann method for fluid flow. *Annu. Rev. Fluid Mech.* **30**, 329–364.

CHIEN, S. 1970 Shear dependence of effective cell volume as a determinant of blood viscosity. *Science* **168**, 977–979.

CHIEN, S., USAMI, S. & BERTLES, J. F. 1970 Abnormal rheology of oxygenated blood in sickle cell anemia. *J. Clin. Invest.* **49**, 623–634.

CLAUSEN, J. R., REASOR, D. A. JR & AIDUN, C. K. 2011 The rheology and microstructure of concentrated non-colloidal suspensions of deformable capsules. *J. Fluid Mech.* **685**, 202–234.

COKELET, G. R. & MEISELMAN, H. J. 1968 Rheological comparison of hemoglobin solutions and erythrocyte suspensions. *Science* **162**, 275–277.

COKELET, G. R. & MEISELMAN, H. J. 2007 Macro and micro rheological properties of blood. In *Handbook of Hemorheology and Hemodynamics*, pp. 45–71. IOS Press.

CORDASCO, D. & BAGCHI, P. 2014 Orbital drift of capsules and red blood cells in shear flow. *Phys. Fluids* **25**, 091902.

CORDASCO, D., YAZDANI, A. & BAGCHI, P. 2014 Comparison of erythrocyte dynamics in shear flow under different stress-free configurations. *Phys. Fluids* **26**, 041902.

DINTENFASS, L. & SOMER, T. 1975 On the aggregation of red cells in Waldenström's macroglobulinaemia and multiple myeloma. *Microvasc. Res.* **9**, 279–286.

DUPIN, M. M., HALLIDAY, I., CARE, C. M., ALBOUL, L. & MUNN, L. L. 2007 Modeling the flow of dense suspensions of deformable particles in three dimensions. *Phys. Rev.* E **75**, 066707.

DUPIRE, J., ABKARIAN, M. & VIALLAT, A. 2010 Chaotic dynamics of red blood cells in a sinusoidal flow. *Phys. Rev. Lett.* **104**, 168101.

DUPIRE, J., SOCOL, M. & VIALLAT, A. 2012 Full dynamics of a red blood cell in shear flow. *Proc. Natl Acad. Sci. USA* **109**, 20808–20813.

EINSTEIN, A. 1911 Berichtigung zu meiner Arbeit:Eine neue Bestimmung der Moleküldimensionen. *Ann. Phys.* **34**, 591–592.

EMBURY, S. H., CLARK, M. R., MONROY, G. & MOHANDAS, N. 1984 Concurrent sickle cell anemia and alpha-thalassemia. Effect on pathological properties of sickle erythrocytes. *J. Clin. Invest.* **73**, 116–123.

EVANS, E., MOHANDAS, N. & LEUNG, A. 1984 Static and dynamic rigidities of normal and sickle erythrocytes. Major influence of cell hemoglobin concentration. *J. Clin. Invest.* **73**, 477–488.

FEDOSOV, D. A., PANB, W., CASWELL, B., GOMPPERA, G. & KARNIADAKIS, G. E. 2011 Predicting human blood viscosity in silico. *Proc. Natl Acad. Sci. USA* **108**, 11772–11777.

FISCHER, T. M. 2004 Shape memory of human red blood cells. *Biophys. J.* **86**, 3304–3313.

FISCHER, T. M., STÖHR-LIESEN, M. & SCHMID-SCHÖNBEIN, H. 1978 The red cell as a fluid droplet: tank tread-like motion of the human erythrocyte membrane in shear flow. *Science* **202**, 894–896.

FOESSEL, É., WALTER, J., SALSAC, A.-V. & BARTHÉS-BIESEL, D. 2011 Influence of internal viscosity on the large deformation and buckling of a spherical capsule in a simple shear flow. *J. Fluid Mech.* **672**, 477–486.

FREUND, J. B. 2007 Leukocyte margination in a model microvessel. *Phys. Fluids* **19**, 023301.

GOLDSMITH, H. L. 1972 The microrheology of human erythrocyte suspensions. In *Proc. 13th IUTAM Congress on Theoretical and Applied Mechanics* (ed. E. Becker & G. K. Mikhailov), pp. 85–103. Springer.

GROSS, M., KRÜGER, T. & VARNIK, F. 2014 Rheology of dense suspensions of elastic capsules: normal stresses, yield stress, jamming and confinement effects. *Soft Matt.* **10**, 4360–4372.

HARKNESS, J. & WHITTINGTON, R. B. 1970 Blood-plasma viscosity: an approximate temperature-invariant arising from generalised concepts. *Biorheology* **6**, 169–187.

HENRÍQUEZ-RIVERA, R. G., SINHA, K. & GRAHAM, M. D. 2015 Margination regimes and drainage transition in confined multicomponent suspensions. *Phys. Rev. Lett.* **114**, 188101.

ISHIKAWA, T. 2012 Vertical dispersion of model microorganisms in horizontal shear flow. *J. Fluid Mech.* **705**, 98–119.

ITO, H., MURAKAMI, R., SAKUMA, S., TSAI, C.-H. D., GUTSMANN, T., BRANDENBURG, K., PÖSCHL, J. M. B., ARAI, F., KANEKO, M. & TANAKA, M. 2017 Mechanical diagnosis of human erythrocytes by ultra-high speed manipulation unraveled critical time window for global cytoskeletal remodeling. *Sci. Rep.* **7**, 43134.

JEFFERY, D. J., MORRIS, J. F. & BRANDY, J. F. 1993 The pressure moments for two rigid spheres in low-Reynolds-number flow. *Phys. Fluids* A **5**, 2317–2325.

JEFFERY, G. B. 1922 The motion of ellipsoidal particles immersed in a viscous fluid. *Proc. R. Soc. Lond.* A **102**, 161–179.

KAUL, D. K. & XUE, H. 1991 Rate of deoxygenation and rheologic behavior of blood in sickle cell anemia. *Blood* **77**, 1353–1361.

KOUTSIARIS, A. G., TACHMITZI, S. V. & BATIS, N. 2013 Wall shear stress quantification in the human conjunctival pre-capillary arterioles *in vivo*. *Microvasc. Res.* **85**, 34–39.

KOUTSIARIS, A. G., TACHMITZI, S. V., BATIS, N., KOTOULA, M. G., KARABATSAS, C. H., TSIRONI, E. & CHATZOULIS, D. Z. 2007 Volume flow and wall shear stress quantification in the human conjunctival capillaries and post-capillary venules *in vivo*. *Biorheology* **44**, 375–386.

KRIEGER, I. M. & DOUGHERTY, T. J. 1959 A mechanism for non-Newtonian flow in suspensions of rigid spheres. *Trans. Soc. Rheol.* **3**, 137–152.

KRÜGER, T., VARNIK, F. & RAABE, D. 2011 Particle stress in suspensions of soft objects. *Trans. R. Soc. Lond.* A **369**, 2414–2421.

KUMAR, A., HENRÍQUEZ-RIVERA, R. G. & GRAHAM, M. D. 2014 Flow-induced segregation in confined multicomponent suspensions: effects of particle size and rigidity. *J. Fluid Mech.* **738**, 423–462.

LANOTTE, L., MAUER, J., MENDEZ, S., FEDOSOV, D. A., FROMENTAL, J.-M., CLAVERIA, V., NICOUL, F., GOMPPER, G. & ABKARIAN, M. 2016 Red cells' dynamic morphologies govern blood shear thinning under microcirculatory flow conditions. *Proc. Natl Acad. Sci. USA* **113**, 13289–13294.

LEES, A. W. & EDWARDS, S. F. 1972 The computer study of transport processes under extreme conditions. *J. Phys.* C **1**, 1921–1928.

LI, J., DAO, M., LIM, C. T. & SURESH, S. 2005 Spectrin-level modeling of the cytoskeleton and optical tweezers stretching of the erythrocyte. *Phys. Fluids* **88**, 3707–6719.

MATSUNAGA, D., IMAI, Y., YAMAGUCHI, T. & ISHIKAWA, T. 2016 Rheology of a dense suspension of spherical capsules under simple shear flow. *J. Fluid Mech.* **786**, 110–127.

MAUER, J., MENDEZ, S., LANOTTE, L., NICOUD, F., ABKARIAN, M., GOMPPER, G. & FEDOSOV, D. A. 2018 Flow-induced transitions of red blood cell shapes under shear. *Phys. Rev. Lett.* **121**, 118103.

MIKI, T., WANG, X., AOKI, T., IMAI, Y., ISHIKAWA, T., TAKASE, K. & YAMAGUCHI, T. 2012 Patient-specific modeling of pulmonary air flow using GPU cluster for the application in medical particle. *Comput. Meth. Biomech. Biomed. Engng* **15**, 771–778.

MOHANDAS, N. & GALLAGHER, P. G. 2008 Red cell membrane: past, present, and future. *Blood* **112**, 3939–3948.

OMORI, T., IMAI, Y., YAMAGUCHI, T. & ISHIKAWA, T. 2012 Reorientation of a non-spherical capsule in creeping shear flow. *Phys. Rev. Lett.* **108**, 138102.

OMORI, T., ISHIKAWA, T., IMAI, Y. & YAMAGUCHI, T. 2014 Hydrodynamic interaction between two red blood cells in simple shear flow: its impact on the rheology of a semi-dilute suspension. *Comput. Mech.* **54**, 933–941.

PEDLEY, T. J. 1980 *The Fluid Mechanics of Large Blood Vessels*. Cambridge University Press.

PENG, Z., MASHAYEKH, A. & ZHU, Q. 2014 Erythrocyte responses in low-shear-rate flows: effects of non-biconcave stress-free state in the cytoskeleton. *J. Fluid. Mech.* **742**, 96–118.

PESKIN, C. S. 2002 The immersed boundary method. *Acta Numerica* **11**, 479–517.

PICANO, F., BREUGEM, W. P., MITRA, D. & BRANDT, L. 2013 Shear thickening in non-Brownian suspensions: an excluded volume effect. *Phys. Rev. Lett.* **111**, 098302.

POZRIKIDIS, C. 1992 *Boundary Integral and Singularity Methods for Linearized Viscous Flow*. Cambridge University Press.

PUIG-DE-MORALES-MARINKOVIC, M., TURNER, K. T., BUTLER, J. P., FREDBERG, J. J. & SURESH, S. 2007 Viscoelasticity of the human red blood cell. *Am. J. Physiol. Cell Physiol.* **293**, C597–C605.

RAMANUJAN, S. & POZRIKIDIS, C. 1998 Deformation of liquid capsules enclosed by elastic membranes in simple shear flow: large deformations and the effect of fluid viscosities. *J. Fluid Mech.* **361**, 117–143.

REASOR, D. A. JR, CLAUSEN, J. R. & AIDUN, C. K. 2013 Rheological characterization of cellular blood in shear. *J. Fluid Mech.* **726**, 497–516.

ROSTI, M. E. & BRANDT, L. 2018 Suspensions of deformable particles in a Couette flow. *J. Non-Newtonian Fluid Mech.* **262C**, 3–11.

ROSTI, M. E., BRANDT, L. & MITRA, D. 2018 Rheology of suspensions of viscoelastic spheres: deformability as an effective volume fraction. *Phys. Rev. Fluids* **3**, 012301.

SCHMID-SCHÖNBEIN, H. & WELLS, R. 1969 Fluid drop-like transition of erythrocytes under shear. *Science* **165**, 288–291.

SECOMB, T. W. 2017 Blood flow in the microcirculation. *Annu. Rev. Fluid Mech.* **49**, 443–461.

SINHA, K. & GRAHAM, M. D. 2015 Dynamics of a single red blood cell in simple shear flow. *Phys. Rev.* E **92**, 042710.

SKALAK, R., TOZEREN, A., ZARDA, R. P. & CHIEN, S. 1973 Strain energy function of red blood cell membranes. *Biophys. J.* **13**, 245–264.

SKOVBORG, F., NIELSEN, A. A. V., SCHLICHTKRULL, J. & DITZEL, J. 1966 Blood-viscosity in diabetic patients. *Lancet* **287**, 129–131.

SOMER, T. 1987 Rheology of paraproteinaemias and the plasma hyperviscosity syndrome. *Bailliére's Clin. Haematol.* **1**, 695–723.

STICKEL, J. J. & POWELL, R. L. 2005 Fluid mechanics and rheology of dense suspensions. *Annu. Rev. Fluid Mech.* **37**, 129–149.

SURESH, S., SPATZ, J., MILLS, J. P., MICOULET, A., DAO, M., LIM, C. T., BEIL, M. & SEUFFERLEIN, T. 2005 Connections between single-cell biomechanics and human diseases states: gastrointestinal cancer and malaria. *Acta Biomater.* **1**, 15–30.

TAKEISHI, N. & IMAI, Y. 2017 Capture of microparticles by bolus of red blood cells in capillaries. *Sci. Rep.* **7**, 5381.

TAKEISHI, N., IMAI, Y., ISHIDA, S., OMORI, T., KAMM, R. D. & ISHIKAWA, T. 2016 Cell adhesion during bullet motion in capillaries. *Am. J. Physiol. Heart Circ. Physiol.* **311**, H395–H403.

TAKEISHI, N., IMAI, Y., NAKAAKI, K., YAMAGUCHI, T. & ISHIKAWA, T. 2014 Leukocyte margination at arteriole shear rate. *Physiol. Rep.* **2**, e12037.

TAKEISHI, N., IMAI, Y. & WADA, S. 2019 Capture event of platelets by bolus flow of red blood cells in capillaries. *J. Biomech. Sci. Engng* (submitted), https://www.jstage.jst.go.jp/article/jbse/advpub/0/advpub_18-00535/_article.

TAKEISHI, N., IMAI, Y., YAMAGUCHI, T. & ISHIKAWA, T. 2015 Flow of a circulating tumor cell and red blood cells in microvessels. *Phys. Rev.* E **92**, 063011.

TAO, R. & HUANG, K. 2011 Reducing blood viscosity with magnetic fields. *Phys. Rev.* E **84**, 011905.

TAYLOR, G. T. 1923 The motion of ellipsoidal particles immersed in a viscous fluid. *Proc. R. Soc. Lond.* A **102**, 58–61.

TAYLOR, G. T. 1932 The viscosity of a fluid containing small drops of another fluid. *Proc. R. Soc. Lond.* A **138**, 41–48.

TSUBOTA, K., WADA, S. & LIU, H. 2014 Elastic behavior of a red blood cell with the membrane's nonuniform natural state: equilibrium shape, motion transition under shear flow, and elongation during tank-treading motion. *Biomech. Model. Mechanobiol.* **13**, 735–746.

UNVERDI, S. O. & TRYGGVASON, G. 1992 A front-tracking method for viscous, incompressible, multi-fluid flows. *J. Comput. Phys.* **100**, 25–37.

USAMI, S., CHIEN, S., SCHOLTZ, P. M. & BERTLES, J. F. 1975 Effect of deoxygenation on blood rheology in sickle cell disease. *Microvasc. Res.* **9**, 324–334.

WALTER, J., SALSAC, A. V., BARTHÉS-BIESEL, D. & TALLEC, P. L. 2010 Coupling of finite element and boundary integral methods for a capsule in a stokes flow. *Intl J. Numer. Meth. Engng* **83**, 829–850.

XIAO, F., HONMA, Y. & KONO, T. 2005 A simple algebraic interface capturing scheme using hyperbolic tangent function. *Intl J. Numer. Meth. Fluids* **48**, 1023–1040.

YOKOI, K. 2007 Efficient implementation of THINC scheme: a simple and practical smoothed VOF algorithm. *J. Comput. Phys.* **226**, 1985–2002.